Sven Peter Näsholm

Ultrasound beams for enhanced image quality

Thesis for the degree of philosophiæ doctor

Trondheim, April 2008

Norwegian University of Science and Technology
Faculty of Medicine
Department of Circulation and Medical Imaging

NTNU

NTNU
Norwegian University of Science and Technology

Thesis for the degree of philosophiæ doctor

Faculty of Medicine
Department of Circulation and Medical Imaging

ISBN 978-82-471-9130-9 (printed version)
ISBN 978-82-471-9144-6 (electronic version)
ISSN 1503-8181

Doctoral thesis at NTNU, 2008-152

Printed by NTNU-trykk

Ultralydstråler for forbedret bildekvalitet

Bildekvaliteten ved bruk av ultralyd i medisinsk diagnostikk varierer mellom ulike organer og fra pasient til pasient. Bedre bildekvalitet forbedrer diagnosepresisjonen og kan føre til mer utbredt anvendelse av ultralyd for eksempel ved bryst- og prostatadiagnose. Utralydpulser genereres av en piezo-elektrisk transduser, som ofte er oppdelt i flere elementer. Den konverterer elektrisk spenning til vibrasjoner som sendes inn i kroppen. Tilbakespredt lyd mottas av transduseren og tolkes til bilder. Mange egenskaper hos et ultralyd-avbildingssystem kan forutsies fra dets sender- og mottakerstråler.

I avhandlingen presenteres og analyseres en ny metode for design av annulære (ringformede) transduserelementer. I stedet for at alle elementer er geometrisk fokusert til samme dybde, er fokuseringen ulik fra element til element. Metoden er gunstig for kombinasjon av store mottakeraperturer og høy lydfrekvens som gir god bildeoppløsning. Samtidig dekker bildet et stort dybdeområde. Et arrayforslag designet med metoden vises, og dets mottakerstråler er beregnet numerisk.

En metode, kalt SURF, for generering av senderstråler som undertrykker reverberasjons-støy blir også analysert. Støyen oppstår pga. uønskede multiple ekkoer når lyd vandrer frem og tilbake mellom sterke reflektorer i vevet. De plukkes opp i det mottatte signalet og kan gjøre bildet tåkete. SURF-metoden er basert på samtidig utsendelse av en høyfrekvent bildepuls og en lavfrekvent manipulasjonspuls. På grunn av en ikke-lineær effekt forandrer den lavfrekvente pulsen lydhastigheten som bildepulsen beveger seg med. Numeriske simuleringer indikerer at SURF-sendestråler kan dannes både i et homogent propagasjonsmedium og når en modell av en sterkt ikke-homogen kroppsvegg er tilstede. Simulerte sendestråler sammenlignes både med stråler ved standard fundamentalavbildning og ved pulsinversjon. I tillegg presenteres en metode for å prosessere motatte SURF-signaler i ettertid til å forandre dybden for maksimal reverberasjonsundertrykkelse.

Resultatene som vises er funnet ved numerisk simulering og teoretisk analyse. De innbyr til utprøving av hvordan metodene yter ved bildedannelse *in vivo*. Til dette kreves nye typer av transduserarrayer. Reverberasjonsundertrykkelse ved SURF bør ytterligere analyseres ved simuleringsmetoder for bølgeforplanting som tar hensyn til multippel spredning. Samlet bidrar avhandlingen til videreutvikling av metoder for å forbedre bildekvaliteten ved medisinsk ultralydundersøkelse.

Sven Peter Näsholm, Institutt for sirkulasjon og bildediagnostikk
Veileder: Bjørn A. J. Angelsen
Finansieringskilde: Norges Forskningsråd, programmet for medisin og helse

Ovennevnte avhandling er funnet verdig til å forsvares offentlig for graden philosophiæ doctor (PhD) i medisinsk teknologi. Disputas finner sted i auditoriet, Medisinsk teknisk forskningssenter, mandag 19. mai 2008, kl. 12:15.

Abstract

The contents of this thesis consider new methods for generating ultrasound beams for enhanced image quality in medical imaging. The results presented are produced through computer simulations. The thesis consists of an introductory chapter and four papers, which are all intended to be individually readable.

Chapter 1 gives a brief overview of ultrasound and medical ultrasound imaging, as well as different aspects of ultrasound image quality and acoustic noise. A non-linear wave equation is presented and analyzed. This equation describes ultrasound propagation within, and interaction with tissue.

In Paper A, a transducer annular array design method is presented. The method involves a geometric pre-focusing, which may vary between the array elements. This is useful for producing narrow receive beams within a large imaging depth window. It is advantageous for avoiding problems that occur when combining high frequencies and large receive apertures when utilizing the conventional equal-area design method.

Paper B introduces a method to produce synthetic transmit beams that are useful for suppression of reverberation noise caused by multiple scattering of the forward-propagating imaging pulse. This is done through combination of two transmit pulse complexes denoted Second order UltRasound Field (SURF). Each such complex consists of a conventional high-frequency imaging pulse added to a low-frequency sound-speed manipulation pulse. The SURF transmit beam is generated by forming the difference between the propagated fields, filtered around the imaging frequency. This beam has suppressed amplitude near the transducer, where

a reflection-generating body-wall is often present during *in vivo* imaging. Furthermore, a method to produce a combined second-harmonic pulse inversion (PI) and SURF beam is also presented, here denoted SURF-PI.

Two imaging setups are defined for which the feasibility of the method is tested through simulations in case of propagation through homogeneous tissue. SURF beams and combined SURF-PI beams are compared to fundamental imaging and PI imaging beams for the two setups. The SURF-PI beams are the most suppressed in the near-field, followed by the approximately equally suppressed SURF and PI beams. The signal level within the imaging depth region becomes higher for SURF than for PI.

In Paper C, two signal processing methods for further adjustment of the SURF beams are introduced. This is achieved through post-processing, either by application of a time-shift, or of a general filter, to one of the propagated fields. The processing is done prior to carrying out the subtraction that is done to form the SURF beam. This provides a flexible way of adjustment to choose the depth position where the scattering sources wished to be suppressed are located. Different adjustments may be realized without need for re-transmission or resumed propagation of the SURF pulse complexes. The post-processing methods are applied to a dataset generated for Paper B. Adjusted transmit beam examples are presented and their reverberation suppression abilities are compared to non-adjusted SURF.

In Paper D, the feasibility study of the SURF beam generation as presented in Paper B, and its post-processing adjustment as presented in Paper C, are enlarged to include propagation within an inhomogeneous medium where a body-wall model producing severe aberration delays is present. It is shown that both the generation of the SURF beams and the post-processing adjustment are attainable under the modeled conditions.

Preface

This thesis is submitted in partial fulfillment of the requirements for the degree of PhD at the Norwegian University of Science and Technology (NTNU). The research was founded by the Research Council of Norway (NFR). It has been supervised by Professor Bjørn A. J. Angelsen and was carried out at the Department of Circulation and Medical Imaging of the Faculty of Medicine, NTNU. The thesis describes work carried out from spring 2003 to summer 2007 concerning ultrasound beams for enhanced quality in medical imaging. It is based on theoretical considerations as well as numerical simulations.

Acknowledgments

My principal gratitude is towards Prof. Bjørn A. J. Angelsen for invaluable guidance and support throughout my work. His knowledge, energy, optimism, never-ending flood of ideas, and belief in me have been of great importance for my motivation to complete this work.

Thanks to Dr. Tonni F. Johansen for always helping me when needed, in particular with explaining and making things clear whenever assistance in unveiling the secrets of ultrasound theory has been necessary.

I want to thank my colleagues at the department for providing such a creative, tolerant and productive environment. I especially mention Jochen Deibele, Dr. Rune Hansen, Halvard Kaupang, Dr. Svein-Erik Måsøy, Øyvind Krølle-Velle Standal and Thor-Andreas Tangen, with whom I have been working in close collaboration. In particular I wish to thank Jochen, Rune and Svein-Erik for help in proof-reading and giving feedback in order to improve my writing.

In addition I want to express my gratitude to Anders Fougner for reviewing the introductory section.

Finally I wish to warmly thank my dear Lisa for love, patience, and encouragements, especially when times were tough for me.

Contents

Chapter 1

Introduction

S. P. Näsholm
Department of Circulation and Medical Imaging, NTNU

Ultra is a Latin prefix meaning *beyond*. Ultrasound [1] is defined as sound with a frequency higher than the upper limit of human hearing, which is approximately 20 kHz. Ultrasound applications include:

- *Medical imaging*, also known as medical ultrasonography [2].
- *Medical therapy*, used *e.g.* for stimulation in physical therapy and breaking up kidney stones. High intensity focused ultrasound (HIFU) is used for localized heating of tissue in order to destroy pathogenic tissue [3, 4].
- *Non-destructive testing*, used to examine and characterize materials, *e.g.* concrete and metals [5, 6].
- *Sound navigation and ranging (SONAR)*, for underwater navigation and detection.
- *Cleaning* of for example teeth, lenses and instruments.

Ultrasound is also used by animals like bats, whales and dolphins for navigation [7].

1.1 Medical ultrasound imaging

1.1.1 Overview

Medical ultrasonography is used in a wide range of areas of patient diagnosis, where maybe obstetrics (woman and unborn child during

pregnancy) and cardiology (heart and blood vessels) are the most well-known to the general public.

The image quality varies greatly between patients and organs. Improved image quality enhances the diagnosis accuracy and has the potential to open up for increased use of ultrasound imaging *e.g.* in breast and prostate cancer diagnosis and screening.

The medical ultrasound imaging modality suits especially well for imaging of soft tissue and muscles. It owes its popularity amongst others to its non-invasive nature, and that the equipment is inexpensive and portable compared to *e.g.* nuclear magnetic resonance (NMR) and X-ray computed tomography (CT). Furthermore, it has no known medical side-effects, and the images are produced in real-time, therefore shortening the delay between patient examination and diagnosis.

Ultrasound waves propagating in human tissue are longitudinal compression waves traveling at about 1540 m/s. The temporal wave frequency utilized for most medical imaging is within the approximate interval from 1 to 15 MHz, corresponding to wavelengths between 1.5 and 0.1 mm.

Conventional ultrasound imaging is based on the pulse-echo technique, which essentially relies on transmission of a pulse, receiving echoes and interpreting them to form an image. The image reconstruction is done assuming the speed of sound to be constant within the object. Measurement of the amplitude of the received echoes, while relating to their respective time-of-flight, makes it possible to map the position of back-scattering targets along the direction of the ultrasound beam. By scanning the ultrasound beam in a plane or a volume, a two-dimensional (2D) or three-dimensional (3D) image is constructed.

The ultrasound pulse is generated by a piezo-electric transducer which converts an applied voltage pulse into the ultrasonic vibration which is transmitted into the body. The back-scattered vibrations are received by the transducer, which converts them into electric signals that are interpreted by the ultrasound scanner to generate the image. The transducer is often divided into an array of individual elements.

1.2.2 Resolution estimates, transmit and receive beams

The *spatial resolution* of an imaging system indicates the minimum distance between two targets in order to be able to distinguish them from each other. The spatial resolution in depth (the *range resolution*), Δz, is proportional to the temporal length T_p of the transmitted pulse: [8]

$$\Delta z \propto cT_p/2, \tag{1.1}$$

where c is the speed of sound. This pulse length is given by the frequency bandwidth. For a constant number of pulse oscillations, this bandwidth is proportional to the frequency. An increase in frequency hence gives better range resolution.

The *lateral resolution* Δr, which is the resolution transverse to pulse propagation direction, is in focus proportional to the spatial wavelength λ times the width of the active aperture: [8]

$$\Delta r \propto F_{\#}\lambda, \tag{1.2}$$

where $F_{\#}$ is the F-number being defined as the ratio between the width of the active aperture and the depth. The frequency is $f = c/\lambda$, so increased frequency hence gives better resolution also laterally.

Another important measure for an ultrasound beam is the depth-of-field L_F, which illustrates the length of the range window where effective imaging is feasible: [9]

$$L_F \propto F_{\#}^2\lambda. \tag{1.3}$$

The *contrast resolution* indicates the minimum ratio there has to be between the scattering strength of two targets in order to make them distinguishable in the image. The contrast resolution gets worse with increased acoustic noise, as discussed in Section 1.3.3.

Many image quality properties in the lateral direction of an ultrasound system are predicted from the *transmit beam* and the *receive beam*. The transmit beam illustrates how the insonification energy from the propagating transmit pulse is distributed in space, while the receive beam illustrates the sensitivity to reception of back-scattering signals from a

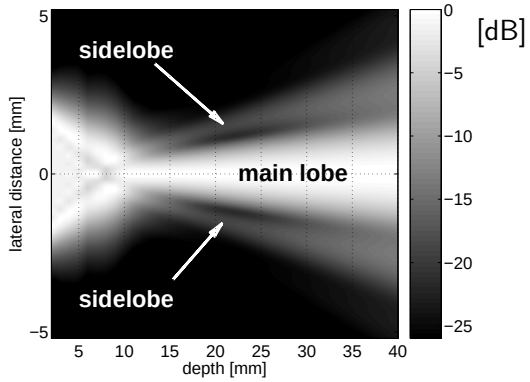

Figure 1.1: Simulated transmit beam example for a 7.5 MHz pulse excitation without apodization, from a focused circular transducer aperture with $\varnothing = 4.8$ mm. The mainlobe and the sidelobes of the beam are indicated. The beam pressure amplitude is shown in decibel.

target depending on its location. Fig. 1.1 shows a transmit beam example, with its mainlobe and first sidelobes indicated.

The reciprocity of the linear wave-equation makes the receive beam equal to the transmit beam if the apertures and pulses are the same. The *two-way beam* for an imaging setup is the product of the transmit and receive beams and indicates much of its lateral pulse-echo imaging properties.

When the ultrasound receive transducer is divided into an array of elements, acquired receive signals from each element may be processed, *e.g.* by application of varying electronic focusing delays, before the total received signal is summed up. This allows use of *dynamic aperture* and *dynamic focusing* allowing the receive beam to be more narrow than the transmit beam.

Dynamic focusing involves a dynamic variation of the electronic delays of the array elements in order to make the receive focus follow reflections from deeper and deeper depths. Application of dynamic aperture means that the number of active receive elements is increased with the imaging depth in order to keep the F-number, and hence the receive beam-width, uniform within the imaging depth window.

1.3.3 Sources of acoustic noise

Medical ultrasound *in vivo* images often show large, patient dependent variation in noise and spatial resolution degradation due to heterogeneous mixtures of fat, muscles, parenchymatic and connective tissue of varying speed of sound being present within the ultrasound propagation path. Such degradation is for example likely to be present when imaging through the abdominal or chest walls. Three important factors regarding noise are: [9, 10]

1. *Wave-front aberration:* The inhomogeneous speed of sound makes different parts of the propagating wave-front experience different speed of sound. This distorts the shape of the wave-front and introduces a variation in its amplitude. Therefore the sidelobe energy is increased, giving worse contrast resolution, and the mainlobe becomes wider, giving worse spatial resolution.

2. *Reverberation:* Heterogeneities produce multiple scattering of the propagating transmit pulse, that is parts of the wave are reflected back and forth several times. Such echoes mix with the main receive signal that is scattered only once. Therefore the contrast resolution is reduced giving a haze noise in the image, and false copies of interfaces may appear at deeper depths than where their true originals are located.

3. *Attenuation:* Several mechanisms, where transformation of wave energy into heat is the most important, makes an ultrasonic pulse lose energy while propagating. As a rule of thumb the attenuation loss in human tissue is $0.5\,\mathrm{dB}/(\mathrm{cm}\cdot\mathrm{MHz})$ [9]. The accumulated attenuation thus grows with the distance covered and increases with frequency. Therefore the deepest depth with acceptable ratio between the signal and the electronic and thermal noise (which are always present within the imaging system), decreases with frequency. It is hence necessary to reduce the frequency, and therefore also the resolution, when imaging at great depths.

In addition, due to the finite size of the transducer aperture, *beam sidelobes* appear in a skirt-shaped pattern around the beam mainlobe, as

shown in Fig. 1.1. They affect the contrast resolution. The sidelobe level may be reduced by introduction of *apodization* through reduction of the vibration amplitude on the edge of the transducer [9]. This enhances the contrast resolution, however at the cost of reduced spatial resolution owing to a widening of the mainlobe.

1.4.4 A non-linear wave equation

Ultrasound non-linear scattering and propagation of a focused beam in heterogeneous tissue may be described by the wave-equation for the momentum potential $\varphi(\vec{r},t)$, connected to the pressure by $p(\vec{r},t) = \dfrac{\partial\varphi(\vec{r},t)}{\partial t}$, and to the particle velocity by $\vec{u}(\vec{r},t) = -\dfrac{\nabla\varphi(\vec{r},t)}{\rho(\vec{r})}$, where $\rho(\vec{r})$ is the mass density, and the spatial respectively temporal coordinates are denoted $\vec{r}$ and t: [11]

$$\underbrace{\nabla^2\varphi(\vec{r},t) - \frac{1}{c^2(\vec{r};p)}\frac{\partial^2\varphi(\vec{r},t)}{\partial t^2}}_{\substack{\text{(A.)}\\ \text{non-linear propagation}}} - \underbrace{h_p \underset{t}{\otimes} \frac{1}{c_0^2}\frac{\partial^2\varphi(\vec{r},t)}{\partial t^2}}_{\substack{\text{(B.)}\\ \text{absorption}}}$$
$$= \underbrace{\frac{\sigma_l(\vec{r})}{c_0^2(\vec{r})}\frac{\partial^2\varphi(\vec{r},t)}{\partial t^2} + \nabla\big(\gamma(\vec{r})\nabla\varphi(\vec{r},t)\big)}_{\substack{\text{(C.)}\\ \text{linear scattering source terms}}} - \underbrace{\frac{\sigma_n(\vec{r};p)}{c_0^2(\vec{r})}\frac{\partial^2\varphi(\vec{r},t)}{\partial t^2}}_{\substack{\text{(D.)}\\ \text{non-linear scattering}\\ \text{source terms}}} . \tag{1.4}$$

The variables σ_l, σ_n and γ denote the linear scattering cross section, the non-linear scattering cross section, and the rapid relative variation in density, and are further described below.

The derivation of Eq. 1.4 is based on a splitting of the spatial variations in density and in the non-linear elastic compressibility function $K(\vec{r};p)$ into spatially slowly and rapidly varying components, compared to the wavelength λ:

$$\rho(\vec{r}) = \underbrace{\rho_a(\vec{r})}_{\substack{\text{slowly}\\ \text{varying}}} + \underbrace{\rho_f(\vec{r})}_{\substack{\text{rapidly}\\ \text{varying}}}, \qquad K(\vec{r};p) = \underbrace{K_a(\vec{r};p)}_{\substack{\text{slowly}\\ \text{varying}}} + \underbrace{K_f(\vec{r};p)}_{\substack{\text{rapidly}\\ \text{varying}}}. \tag{1.5}$$

The total elastic compressibility function is in soft tissue approximated to the second order of pressure by

$$K(p) \approx (1 - \beta_n \kappa p)\, \kappa p \qquad \Big(= \underbrace{\kappa \cdot p}_{\text{linear}} - \underbrace{\beta_n \kappa^2 \cdot p^2}_{\text{non-linear}} \Big), \tag{1.6}$$

where p is the pressure, β_n a nonlinearity parameter[†], and κ the linear bulk compressibility of the tissue. Then the slowly and rapidly varying components of $K(\vec{r}; p)$ are divided into linear and non-linear parts:

$$K_a(\vec{r}; p) = \underbrace{\kappa_a(\vec{r})p}_{\substack{\text{slow}\\ \text{linear}}} - \underbrace{K_{na}(\vec{r}; p)}_{\substack{\text{slow}\\ \text{non-linear}}}, \qquad K_f(\vec{r}; p) = \underbrace{\kappa_f(\vec{r})p}_{\substack{\text{rapid}\\ \text{linear}}} - \underbrace{K_{nf}(\vec{r}; p)}_{\substack{\text{rapid}\\ \text{non-linear}}}. \tag{1.7}$$

Now the variables in (1.4) may be explained. The squares of the pressure-dependent and the ambient pressure sound speeds $c^2(\vec{r}; p)$ and $c_0^2(\vec{r})$ are

$$c^2(\vec{r}; p) = \frac{1}{\rho_a(\vec{r}) K_a'(\vec{r}; p)}, \quad c_0^2 = \frac{1}{\rho_a(\vec{r}) \kappa_a(\vec{r})}, \tag{1.8}$$

where $K_a'(\vec{r}; p) \triangleq \dfrac{\partial K_a(\vec{r}; p)}{\partial p}$. Combining this definition with (1.6) yields

$$K_a'(\vec{r}; p) \approx \kappa_a - 2\beta_n \kappa_a^2 p. \tag{1.9}$$

The relative rapid variation of the density, the linear scattering cross-section, and the non-linear scattering cross-section are

$$\gamma(\vec{r}) = \frac{\rho_f(\vec{r})}{\rho(\vec{r})}, \qquad \sigma_l(\vec{r}) = \frac{\kappa_f(\vec{r})}{\kappa_a(\vec{r})}, \qquad \sigma_n(\vec{r}; p) = \frac{K_{nf}'(\vec{r}; p)}{\kappa_a(\vec{r})}. \tag{1.10}$$

1.5.5 Approximations in conventional ultrasound image reconstruction

The calculations conventionally performed to construct an ultrasound image are based on a number of approximations that hold to a variable

[†]Beyer [12] defined the nonlinearity parameter as the quotient B/A between the first and second coefficients of the Taylor development of the non-linear wave equation. $\beta_n \triangleq 1 + \frac{B}{2A}$.

extent. The accuracy of the approximations differs between patients and between parts of the body. Some aspects of such approximations are listed below:

1. *Homogeneous speed of sound:* Conventional focusing and beamforming are done under assumption that the speed of sound $c(\vec{r};p)$ and $c_0(\vec{r})$ of Eq. 1.4 have no spatial variation. The presence of a significant spatial variation, *e.g.* due to propagation through a body-wall, does however introduce focus degradation through wave-front aberrations, as described in Section 1.3.3. Refs. 13–18 consider various methods to achieve aberration correction.

2. *Negligible multiple scattering:* The spatial variation in compressibility and density, as stated in Eq. 1.4, give rise to the linear back-scattered signal normally utilized to reconstruct the ultrasound image. When assuming the scattering to be weak, only first-order scattering is significant, making the Born approximation valid [10]. However, in many imaging situations the higher-order scattering is significant, therefore causing reverberation noise, as discussed in Section 1.3.3.

3. *Limited utilization of non-linear propagation effects:* Effects introduced by the pressure-dependency of the speed of sound $c(\vec{r};p)$, in the non-linear propagation part (A.) of Eq. 1.4, are in conventional ultrasound pulse-echo image reconstruction only utilized to a limited extent: for generation of higher harmonics used in the tissue harmonic imaging method, as described in Section 1.6.6.

4. *Limited utilization of non-linear scattering:* The non-linear scattering source-terms (D.) of Eq. 1.4 are explicitly utilized only during detection of the non-linear back-scattering from contrast agents, as reported in Section 1.7.7.

There is potential gain in new methods for ultrasound image reconstruction, if deeper understanding and utilization of the phenomena described by the non-linear wave equation (1.4) are obtained.

1.6.6 Tissue harmonic imaging

Due to the non-linear relation between pressure and tissue density, as shown in Section 1.4.4, the speed of sound is higher for high than for low pressures. This makes the shape of a pulse change during propagation, because its troughs and crests go slower respectively faster than its regions of lower pressure amplitude. The pulse is self-distorted and a fraction of its energy is transferred into harmonic frequencies, that is multiples of the transmit frequency. The change in sound speed, and therefore the amount of energy pumped into higher harmonics, is proportional to the square of the fundamental pressure. For very low amplitudes the distortion is hence negligible, but for amplitudes used in diagnostic imaging, a significant amount of harmonic energy is accumulated during forward-propagation. The higher harmonic components of the pulse are utilized for tissue harmonic imaging (THI) by transmission around the frequency f and receive filtering at the frequency $2f$. THI is in many imaging situations beneficial for generating sharper images thanks to reverberation suppression, aberration reduction, grating lobe decrease and sidelobe suppression [19–23]. Drawbacks of THI imaging at the frequency $2f$, compared to fundamental imaging (by transmission and reception at $2f$) include: decreased signal-to-noise ratio causing reduced penetration depth or reduced highest usable frequency, low near-field signal, reduced range (depth) resolution due to longer pulses, and interference by fundamental frequencies within the receive filter around $2f$ [24]. The first and the last of the mentioned disadvantages are reduced by use of the pulse inversion technique [25].

1.7.7 Second harmonic ultrasound contrast agent imaging

Local non-linear scattering effects are utilized for detection of ultrasound contrast agents. Such agents are gas-filled microbubbles with a typical equilibrium diameter around $1-7\,\mu$m that are injected into the bloodstream [26, 27]. The bubbles oscillate under insonification, so by tracking the agents, imaging of blood flow and blood perfusion into organs is facilitated, especially at low flow speeds. Back-scattering from such gas-bubbles is strongly non-linear [28, 29].

By reconstruction of the image based on higher harmonic frequency components of the echoes, signals from the bubbles may be differentiated from signals from tissue as long as the transmit pulse amplitude is low enough to make the harmonics accumulated within the forward-propagating beam insignificant. Regulation of the ultrasound energy is also important since contrast agent destruction occurs beyond some threshold pressure [30, 31]. Intentional agent destruction may be utilized for drug delivery [32] and for blood flow measurement [33].

Pulse inversion was first utilized in contrast agent detection and helps increase the contrast-to-tissue signal ratio [34–36]. The scattering response from ultrasound contrast agent is described by the Rayleigh-Plesset differential equation [37, 38], and later by more sophisticated models as exemplified in Refs. 39–43.

1.2 Thesis outline

The research presented consists of theoretical developments and numerical computer simulations of ultrasound propagation to form transmit- and receive beams. This is achieved by use of recently developed, and here presented methods.

The remainder of the thesis is made up of four separate papers. Each Paper A–D is written in form of a separate article submitted or intended to be submitted for journal publishing, and should hence be possible to read independently. Therefore some of the contents appear repeatedly, especially in the closely related Papers B–D.

The work performed has increased the conceptual understanding of the investigated subjects and should be followed up by experimental work to prove the feasibility of the methods in real imaging situations.

Paper A treats a method for annular array design to improve the receive beam by combination of high frequency, large aperture and large imaging depth window. It is relevant mainly for imaging when the approximations 1.–2. listed in Section 1.5.5 are accurate. In such cases where the objects are stationary, an increase in image quality is mainly attained by having the best possible spatial resolution. The method is especially useful in 3D imaging with need to make any-plane cuts to study the collected 3D data-

set. To make the quality of such any-plane cuts equal no matter their angle and position, the resolution in azimuth, elevation and range directions need to be similar.

Paper B–D treat a transmit beam generation method denoted Second order UltRasound Field (SURF) reverberation suppression imaging. It utilizes the non-linear propagation effect introduced by term (A.) of Eq.1.4 through application of a low-frequency pulse in addition to the imaging pulse. This enables a new manner to construct transmit beams, which may be utilized for imaging with low sensitivity to a class of reverberation noise. The reverberation suppression property is further emphasized by utilization of a combined SURF and pulse inversion transmit beam.

Below follows a brief description of the individual Papers A–D:

Paper A

An annular array design proposal with multiple geometric pre-foci, is about a developed ultrasound transducer design method denoted multi-focus annular array, which suggests a solution for how to simultaneously combine a large receive aperture with high frequency and a large receive imaging depth window. This way one may attain high resolution combined with a large imaging depth window, within a homogeneous enough medium, *e.g.* in transvaginal fetus imaging. The annular array design method is described and utilized for definition of an array proposal. The geometric pre-focus, realized by curving or by use of an acoustic lens, varies among the annuli. Element sizes and geometric pre-focus depths are determined by a maximum allowed phase-shift within the active depth region of each element, resulting in fewer elements or larger apertures compared to the standard equal area design. The developed design rules are utilized to define an array for imaging within the frequency interval $[7.5, 15]$ MHz. Its total aperture diameter is 22 mm and the thinnest element is 0.23 mm wide. Receive beams resulting from this array are simulated. The beams and their sidelobe to mainlobe energy ratios are compared to an ideally focused reference where there are no phase-shifts over the elements. The sidelobe to mainlobe energy ratio, is within nearly the entire imaging depth window at its worst 5 dB higher than for the ideal reference.

Paper B

Transmit beams adapted to multiple scattering noise suppression using SURF dual-frequency imaging,
introduces the SURF reverberation suppression method. This method utilizes excitation pulse complexes of widely separated frequency bands to suppress noise caused by multiple scattering in medical ultrasound imaging. The pulse complexes are transmitted and propagated to generate a SURF imaging synthetic transmit beam. This beam has reduced amplitude near the transducer, which illustrates the multiple scattering suppression ability of the presented imaging method. Field simulations solving a non-linear wave equation are used to calculate SURF imaging beams, which are compared to beams for pulse inversion (PI) and fundamental imaging. In addition, a combined SURF and PI beam generation method is described and compared to the beams mentioned above. A quality ratio is defined, which relates the energy within the near field to the energy within the imaging region. It is used to score the multiple scattering suppression abilities of imaging when utilizing the different beams. The realized combined SURF-PI beam scores highest, followed by SURF, PI (who score equally well), and the fundamental. The beam amplitude in the imaging region, and hence also the signal-to-noise ratio (SNR), is highest for the fundamental, followed by SURF, PI and SURF-PI. The work thus indicates that when substituting PI for SURF, one may trade-off the increased SNR into use of increased imaging frequencies, without loss of multiple scattering suppression.

Paper C

Post-processing adjustment of the SURF reverberation noise suppression depth,
presents and analyzes two related methods aiming for further enhancement and adjustment of SURF multiple scattering (reverberation) noise suppression in medical ultrasound imaging. The methods solely involve post-processing of the propagated imaging high frequency pulse fields. The same dual-frequency transmit pulse complexes are thus utilized as in non-adjusted SURF reverberation suppression imaging. The post-processing

involves application of an operator, *e.g.* a time-shift, in order to equalize two SURF imaging pulses at a chosen depth. This depth is typically where the first scattering occurs of the reverberation noise that one aims to suppress. The methods are tested on simulated data resulting from propagation of dual-frequency pulse complexes with a 3.5 MHz high frequency imaging pulse in conjunction with a 0.5 MHz low frequency manipulation pulse. Transmit beams are constructed with and without adjustment. In an imaging situation utilizing SURF, the adjustment methods would be applied to the received RF data.

The transmit beams realized using the presented adjustment methods show strong energy decrease at the chosen depth of suppressed first scattering, especially in case of shallow depths, where a body-wall traversed by the beam is often located. The methods are also shown to be useful for reduction of the total SURF transmit beam energy in the near-field compared to within the imaging region. The adjustments may therefore be utilized to attain a slightly better general suppression of multiple scattering noise.

Paper D

SURF reverberation suppression transmit beam generation and post-processing adjustment within an aberrating medium,
contains additional computer simulations of SURF reverberation suppression transmit acoustic imaging fields. They are performed for a propagation path including a strongly aberrating body-wall model. The utilized SURF transmit dual-frequency pulse complexes are similar as in Paper C.

Furthermore, the feasibility of the two signal post-processing methods, presented and tested for a homogeneous medium in Paper C, are investigated within the modeled inhomogeneous medium.

The request of the study arises from the fact that imaging situations where reverberation suppression is useful are also likely to produce pulse wave-front aberrations. Such distortions could potentially produce time-delays that cancel the accumulated propagation time-delay needed for the SURF reverberation suppression technique.

Results show that both the generation of synthetic SURF reverberation suppression imaging transmit beams, and the following post-processing

adjustments, are attainable even though the modeled body-wall introduce time-delays which are larger than previously reported delays measured on human body-wall specimens.

1.3 Summary of contributions

This thesis has four main contributions, which are all analyzed using numerical simulations:

1. A set of new annular array element focusing and size rules are developed. They share with the equal area (EA) design the basic ideas of (i) avoiding the phase-shift over an element to exceed a chosen limit and (ii) controlling the width of the receive beam. However the geometric pre-focusing varies among the elements, enabling their area to be unequal and to be expanded compared to for EA.

2. The SURF reverberation suppression imaging method is presented. The feasibility of generating the corresponding synthetic transmit beam is confirmed through simulations, both in homogeneous medium and with a strongly aberrating body-wall present.

3. The combined SURF and pulse inversion reverberation suppression imaging method is introduced. The feasibility of generating the corresponding synthetic transmit beam is confirmed through simulations within a homogeneous medium.

4. A post-processing method for adjustment of the SURF transmit beam is developed. Its performance is analyzed both in case of a homogeneous medium and in case of an aberrating body-wall being present.

1.4 Suggestions for further work

This thesis presents theoretical analysis and numerical simulation studies regarding new methods to generate ultrasound beams. An obvious further step towards prediction of their clinical benefits is to test them on *in vivo*

data. For this, the data acquisition needed requires manufacturing of new kinds of transducer arrays.

The simulation studies of SURF and SURF-PI may be further investigated regarding reverberation suppression, if a non-linear wave equation solver which takes multiple scattering into consideration is utilized, instead of the pure forward-propagation method used within this work.

The versatility of the SURF pulse complexes opens up for a new set of ultrasound detection methods where the medium-manipulation abilities of its low-frequency pulse are utilized. So far, only a contrast agent detection ability, as demonstrated in Refs. 11, 44–46, and the reverberation suppression method, demonstrated within this work, are published.

References

[1] T. G. Leighton, "What is ultrasound?" *Prog. Biophys. Mol. Biol.*, vol. 93, pp. 3–83, 2007.

[2] P. N. T. Wells, "Ultrasound imaging," *Phys. Med. Biol.*, vol. 51, pp. R83–R98, June 2006.

[3] K. D. Evans, B. Weiss, and M. Knopp, "High-intensity focused ultrasound (HIFU) for specific therapeutic treatments: A literature review," *J. Diagn. Med. Sonog.*, vol. 23, no. 6, pp. 319–327, 2007.

[4] T. J. Dubinsky, C. Cuevas, M. K. Dighe, O. Kolokythas, and J. H. Hwang, "High-intensity focused ultrasound: Current potential and oncologic applications," *Am. J. Roentgenol.*, vol. 190, no. 1, pp. 191–199, Jan. 2008.

[5] F. A. Firestone, "The supersonic reflectoscope, an instrument for inspecting the interior of solid parts by means of sound waves," *J. Acoust. Soc. Am.*, vol. 17, no. 3, pp. 287–299, Jan. 1946.

[6] C. H. Desch, D. O. Sproule, and W. J. Dawson, "The detection of cracks in steel by means of supersonic waves," *J. Iron Steel Inst.*, vol. 153, pp. 319–327, 1946.

[7] G. Jones, "Echolocation," *Curr. Biol.*, vol. 15, pp. R484–R488, July 2005.

[8] M. Arditi, W. B. Taylor, F. S. Foster, and J. W. Hunt, "An annular array system for high resolution breast echography," *Ultrasonic Imaging*, vol. 4, pp. 1–31, 1982.

[9] B. Angelsen, *Ultrasound imaging. Waves, signals and signal processing.* Trondheim: Emantec, 2000, vol. I, http://www.ultrasoundbook.com.

[10] ——, *Ultrasound imaging. Waves, signals and signal processing.* Trondheim: Emantec, 2000, vol. II, http://www.ultrasoundbook.com.

[11] B. A. J. Angelsen and R. Hansen, "SURF imaging – a new method for ultrasound contrast agent imaging," in *Proc. IEEE Ultrason. Symp.*, New York, NY, USA, Oct. 2007, pp. 531–541.

[12] R. T. Beyer, "Parameter of nonlinearity in fluids," *J. Acoust. Soc. Am.*, vol. 32, no. 6, pp. 719–721, 1960.

[13] L. F. Nock, G. E. Trahey, and S. W. Smith, "Phase aberration correction in medical ultrasound using speckle brightness as an image quality factor," *J. Acoust. Soc. Am.*, vol. 85, no. 5, pp. 1819–1833, May 1989.

[14] G. C. Ng, S. S. Worrell, P. D. Freiburger, and G. E. Trahey, "A comparative evaluation of several algorithms for phase aberration correction," *IEEE Trans. Ultrason. Ferroelectr. Freq. Control*, vol. 41, no. 5, pp. 631–643, Sept. 1994.

[15] T. D. Mast, A. I. Nachman, and R. C. Waag, "Focusing and imaging using eigenfunctions of the scattering operator," *J. Acoust. Soc. Am.*, vol. 102, no. 2, pp. 715–725, Aug. 1997.

[16] M. Tabei, T. D. Mast, and R. C. Waag, "Simulation of ultrasonic focus aberration and correction through human tissue," *J. Acoust. Soc. Am.*, vol. 113, no. 2, pp. 1166–1176, 2003.

[17] T. Varslot, H. Krogstad, E. Mo, and B. Angelsen, "Eigenfunction analysis of stochastic backscatter for characterization of acoustic aberration in medical ultrasound imaging," *J. Acoust. Soc. Am.*, vol. 115, no. 6, pp. 3068–3076, June 2004.

[18] S.-E. Måsøy, T. Varslot, and B. Angelsen, "Iteration of transmit-beam aberration correction in medical ultrasound imaging," *J. Acoust. Soc. Am.*, vol. 117, no. 1, pp. 450–461, 2005.

[19] M. A. Averkiou, D. N. Roundhill, and J. E. Powers, "A new imaging technique based on the nonlinear properties of tissue," in *Proc. IEEE Ultrason. Symp.*, 1997, pp. 1561–1566.

[20] B. Ward, A. C. Baker, and V. F. Humphrey, "Nonlinear propagation applied to the improvement of resolution in diagnostic medical ultrasound," *J. Acoust. Soc. Am.*, vol. 101, no. 1, pp. 143–154, 1997.

[21] J. D. Thomas and D. N. Rubin, "Tissue harmonic imaging: why does it work?" *J. Am. Soc. Echocardiogr.*, vol. 11, no. 8, pp. 803–808, 1998.

[22] F. A. Duck, "Nonlinear acoustics in diagnostic ultrasound," *Ultrasound Med. Biol.*, vol. 28, no. 1, pp. 1–18, 2002.

[23] T. Varslot, S.-E. Måsøy, T. F. Johansen, and B. Angelsen, "Aberration in nonlinear acoustic wave propagation," *IEEE Trans. Ultrason., Ferroelectr., Freq. Contr.*, vol. 54, no. 3, pp. 470–479, Mar. 2007.

[24] W. R. Hedrick and L. Metzger, "Tissue harmonic imaging: A review," *J. Diagn. Med. Sonog.*, vol. 21, no. 3, pp. 183–189, 2005.

[25] P. Jiang, Z. Mao, and J. Lazenby, "A new tissue harmonic imaging scheme with better fundamental frequency cancellation and higher signal-to-noise ratio," in *Proc. IEEE Ultrason. Symp.*, vol. 2, 1998, pp. 1589–1594.

[26] D. Cosgrove, "Ultrasound contrast agents: An overview," *Eur. J. Radiol.*, vol. 60, pp. 324–330, Dec. 2006.

[27] E. Quaia, "Microbubble ultrasound contrast agents: an update," *Eur. Radiol.*, vol. 17, pp. 1995–2008, 2007.

[28] N. de Jong, R. Cornet, and C. T. Lancée, "Higher harmonics of vibrating gas-filled microspheres. Part one: Simulations," *Ultrasonics*, vol. 32, no. 6, pp. 447–453, 1994.

[29] ——, "Higher harmonics of vibrating gas-filled microspheres. Part two: Measurements," *Ultrasonics*, vol. 32, no. 6, pp. 455–459, 1994.

[30] J. Chomas, P. Dayton, J. Allen, K. Morgan, and K. Ferrara, "Mechanisms of contrast agent destruction," *IEEE Trans. Ultrason. Ferroelectr. Freq. Control*, vol. 48, no. 1, pp. 232–248, Jan. 2001.

[31] W.-S. Chen, T. J. Matula, A. A. Brayman, and L. A. Crum, "A comparison of the fragmentation thresholds and inertial cavitation doses of different ultrasound contrast agents," *J. Acoust. Soc. Am.*, vol. 113, no. 1, pp. 643–651, Jan. 2003.

[32] S. Bloch, P. Dayton, and K. Ferrara, "Targeted imaging using ultrasound contrast agents," *IEEE Eng. Med. Biol.*, vol. 23, no. 5, pp. 18–29, Sep.–Oct. 2004.

[33] K. Wei, A. R. Jayaweera, S. Firoozan, A. Linka, D. M. Skyba, and S. Kaul, "Quantification of myocardial blood flow with ultrasound-induced destruction of microbubbles administered as a constant venous infusion," *Circulation*, vol. 97, pp. 473–483, Feb. 1998.

[34] D. Simpson and P. Burns, "Pulse inversion doppler: a new method for detecting nonlinear echoes from microbubble contrast agents," *1997 IEEE Ultrason. Symp.*, vol. 2, pp. 1597–1600, Oct. 1997.

[35] K. Morgan, M. Averkiou, and K. Ferrara, "The effect of the phase of transmission on contrast agent echoes," *IEEE Trans. Ultrason. Ferroelectr. Freq. Control*, vol. 45, no. 4, pp. 872–875, July 1998.

[36] L. Hoff, "Nonlinear response of sonazoid. Numerical simulations of pulse-inversion and subharmonics," *2000 IEEE Ultrason. Symp.*, vol. 2, pp. 1885–1888, Oct. 2000.

[37] Lord Rayleigh, "On the pressure developed in a liquid during the collapse of a spherical cavity," *Philos. Mag.*, vol. 34, pp. 94–98, 1917.

[38] M. Plesset, "The dynamics of cavitation bubbles," *J. Appl. Mech.*, vol. 16, pp. 277–282, 1949.

[39] P. J. A. Frinking and N. de Jong, "Acoustic modeling of shell-encapsulated gas bubbles," *Ultrasound Med. Biol.*, vol. 24, pp. 523–533, May 1998.

[40] B. A. J. Angelsen, T. F. Johansen, and L. Hoff, "Simulation of gas bubble scattering for large mach-numbers," in *Proc. IEEE Ultrason. Symp.*, vol. 1, Caesars Tahoe, NV, USA, 1999, pp. 505–508.

[41] L. Hoff, P. C. Sontum, and J. M. Hovem, "Oscillations of polymeric microbubbles: Effect of the encapsulating shell," *J. Acoust. Soc. Am.*, vol. 107, no. 4, pp. 2272–2280, 2000.

[42] D. B. Khismatullin, "Resonance frequency of microbubbles: Effect of viscosity," *J. Acoust. Soc. Am.*, vol. 116, no. 3, pp. 1463–1473, 2004.

[43] E. Klaseboer and B. C. Khoo, "A modified rayleigh-plesset model for a non-spherically symmetric oscillating bubble with applications to boundary integral methods," *Eng. Anal. Bound. Elem.*, vol. 30, pp. 59–71, 2006.

[44] R. Hansen, "New techniques for detection of ultrasound contrast agents," Ph.D. dissertation, Norwegian University of Science and Technology, 2004.

[45] A. Bouakaz and N. de Jong, "New contrast imaging method using double frequency exposure," in *2004 IEEE Ultrason. Symp.*, vol. 1, Aug. 23–27, 2004, pp. 339–342.

[46] S.-E. Måsøy, Ø. Standal, P. Näsholm, T. F. Johansen, R. Hansen, and B. Angelsen, "SURF imaging: In vivo demonstration of an ultrasound contrast agent detection technique," *IEEE Trans. Ultrason. Ferroelectr., Freq. Contr.*, 2008, accepted for publishing.

Paper A

An annular array design proposal with multiple geometric pre-foci[†]

S. P. Näsholm, T. F. Johansen, and B. A. J. Angelsen
Department of Circulation and Medical Imaging, NTNU

An annular array design method is described and utilized for definition of an array proposal. The geometric pre-focus, realized by curving or use of an acoustic lens, varies among the annuli. Element sizes and geometric pre-focus depths are determined by a maximum allowed phase-shift within the active depth region of each element on receive, resulting in fewer elements or larger apertures compared to the standard equal area design. The method allows combination of large aperture and high frequency with a large receive imaging window. The developed design rules are utilized to define an array for imaging within the frequency interval $[7.5, 15]$ MHz. Its total aperture diameter is 22 mm and the thinnest element is 0.23 mm wide. Receive beams resulting from this array are simulated. The beams and their sidelobe to mainlobe energy ratios are compared to an ideally focused reference where there are no phase-shifts over the elements. Within nearly the entire imaging window, the sidelobe to mainlobe energy ratio is less than 5 dB higher than for the ideal reference .

A.1 Introduction

Current ultrasound systems use linear arrays that produce an electronically depth steered receive beam focus (dynamic focusing) within the two-dimensional (2D) image plane (azimuth direction), while normal to the 2D image plane (elevation direction) the beam is poorly focused at a fixed depth. In many 2D imaging

[†]Submitted to *IEEE Transactions on Ultrasonics, Ferroelectrics and Frequency Control* for publishing

situations the limited elevation focusing is acceptable, because one selects for the diagnosis cross section images of a close to cylindrical object (*e.g.* a vessel, a fetal trunk, a heart ventricle). However, when the object is small in all directions, like a small tumor, a small cyst, a young fetal ventricle, the limited elevation focusing produces noise in the images and limits their diagnostic quality.

The limited elevation focusing becomes even more degraded in three-dimensional imaging, where one collects volume data from the object and examines the data by selecting 2D image slices at free angles to the ultrasound beam. When the selected 2D image plane has a skewed angle to the beam, the poor elevation focus shows as highly reduced resolution.

Hence, for adequate three-dimensional volume imaging of objects, and also to visualize small objects, strongly and symmetrically focused ultrasound beams are preferable. This can for example be achieved with 2D arrays which however introduce large instrument complexity.

The annular array allows for symmetric focusing with a small number of elements and thus relatively low instrument complexity. It needs to be mechanically scanned to produce a B-mode image. However, to combine the large aperture needed for narrow beams with a large receive imaging window, current equal area (EA) element designs produce narrow outer elements with complex vibration patterns. This phenomenon puts a practical limit on the maximal aperture that can be achieved with EA annular arrays. Design of pre-focused spherical annular arrays and an introduction to use the EA design are given in [1].

Single element pre-focused transducers are common in high frequency imaging of *e.g.* the human eye, arteries, skin, and laboratory animals like mice [2, 3]. However, large aperture single element transducers suffer from having a short imaging window, being approximately proportional to the wavelength times the squared F-number $F_\#$ [4, 5], where $F_\#$ is the ratio between focal depth and aperture diameter.

A design of an annular array system for high resolution breast echography is described in [4]. Rules for design of an EA array including expressions for the lateral resolution, the imaging window and phase-shift over an element are also given. The EA geometry is also known as a Fresnel plate and is formulated, but not explicitly denoted EA, for ultrasound transducers in [6]. EA elements are described also in [7] for dynamically focused annular arrays.

Recent publications describing annular array designs include a 10 MHz, 8 element array with a 30 mm aperture adapted to detection of tissue motion and strain [8], a 50 MHz 7 element array having an aperture diameter of 2 mm [9], a 40 MHz 5 elements array with a 6 mm aperture [10, 11] and a 6 element 45 MHz array with a 3 mm aperture [12, 13]. A kerfless array with 8 elements with a center frequency of 55 MHz and a total aperture of 3.12 mm is presented in [14]. These

designs either have a short imaging window or high $F_{\#}$, which may be adverse in an imaging situation.

The multi-focus array design method presented here enables simultaneous use of large apertures and high frequencies without need of a large number of thin elements or a short imaging window. This paper is organized as follows: First comes an overview of equations used for annular array design. Afterwards follows an explanation of the multi-focus design method, giving the geometric pre-focus and the size of each element depending on how the receive beamwidth is set to develop with depth. Design rules adapted to a frequency band limited transducer are used to define a multi-focus array. Simulations of dynamically focused receive beams from the proposed array are then performed and compared to (i) the ideal case with no phase-shifts over the array elements and (ii) an EA array with the same number of elements and total aperture as the proposed multi-focus array.

A.2 Annular array design basics

A.1.1 Phase-shift over an element

The geometry of a single annular array element is sketched in Fig. A.1. The maximum propagation time difference $\Delta\tau_j(z)$ and the corresponding phase-shift $\Delta\varphi_j(z) = 2\pi f \Delta\tau_j(z)$ from a point z on the beam axis to two different points on array annulus number j (with geometric pre-focus at F_j), stems from the propagation distance difference $\Delta\ell_j = \ell_o - \ell_i$. This propagation time difference then becomes $\Delta\tau_j(z) = [\ell_o(z) - \ell_i(z)]/c$, where c is the speed of sound.

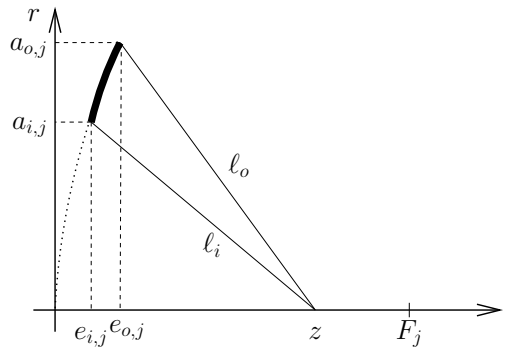

Figure A.1: Element j focused at F_j. Outer and inner radii are $a_{o,j}$ and $a_{i,j}$.

Assuming $a_{o,j}^2 << F_j^2$, the phase-shift due to $\Delta\tau_j$ is [4]

$$\Delta\varphi_j(z) \approx 2\pi \frac{f}{c} \frac{A_j}{2\pi F_j} \frac{F_j - z}{z} = \frac{A_j}{\lambda} \left(\frac{1}{z} - \frac{1}{F_j} \right), \tag{A.1}$$

where A_j is the element area and λ the wavelength. This confirms that $\Delta\varphi_j(z)$ is equal over EA elements.

Large phase-shift over an element causes high sidelobes and efficiency decrease since energy is transferred from the mainlobe to the sidelobes. For EA annular array design with a given number of elements, the choice of largest acceptable phase-shift $\theta \equiv \max(\Delta\varphi_j(z))$ is thus a trade-off between having a narrow beam and low sidelobes. A thorough investigation of the relation between $\Delta\varphi_j$ and element efficiency is given in [15]. There the element is divided into a large number of EA subelements $i = 1 \ldots N$ thin enough to make $\Delta\varphi_i(z)$ insignificant. Its efficiency η is defined as the ratio between the output signal amplitude of the real element and the sum of the signals from the thin subelements $1 \ldots N$:

$$\eta = \frac{\sin(\Delta\varphi_j)}{\Delta\varphi_j} \cdot 100\%. \tag{A.2}$$

For ultimate θ selection, also factors such as imaging situation and transducer frequency bandwidth should be considered. Yuan [15] suggests $\theta = 90°$, which gives $\eta = 64\%$, while Arditi [4] uses $\theta = 133.5°$, which yields $\eta = 31\%$. For the design example presented below, $\theta = 90°$ is chosen.

A.2.2 Beamwidth estimate

The beamwidth in focus can be approximated as [16]

$$d(z) \approx 2\lambda F_{\#} = \lambda \frac{z}{a(z)}, \tag{A.3}$$

where $a(z)$ is the active aperture radius at the depth z, and λ the wavelength.

A.3.3 Penetration depth

The higher the frequency, the higher is the attenuation and the shorter is the ultrasound penetration depth in tissue. As an approximation, the penetration depth d_p, that is the maximum depth where imaging is feasible with acceptable signal-to-noise ratio, is proportional to the wavelength: $d_p = \chi\lambda$, where χ as a rule of thumb is $\sim$300. The shortest λ meaningful to use at the depth z is hence

$$\lambda(z) = z/\chi. \tag{A.4}$$

A.3 Multi-focus array design methods

A.1.1 Overview

The multi-focus array design demands (i) a dynamic receive aperture, (ii) dynamic focusing on receive and (iii) a geometric pre-focus which may differ between the elements. In addition, the electronic circuits connected to the elements must be able to handle non-equal element areas and thus non-equal electric impedances.

The design assumes an expanding receive aperture with element-per-element insertion into the array. Each element size is chosen as large as possible while keeping the maximum phase-shift over it below the limit θ, within its active depth region. For a new element $(j+1)$, the nearest depth $F_{n,j+1}$, where it is part of the active dynamic aperture, is set depending on a chosen beamwidth limitation. Then the outer aperture radius $a_{o,j+1}$ and the geometric pre-focus F_{j+1} are determined as function of outer aperture of the previously inserted element j, element activation depth, maximum total imaging region depth, maximum acceptable phase-shift, and kerf. A summary of the derived equations for F_{j+1} and $a_{o,j+1}$ is given in Tab. A.1. For the proposed design method the elements are grouped into (i) a central conventional EA group and (ii) an outer multi-focus group:

(i) All elements $j = 1 \dots M$ within the central region are designed in an EA manner with equal element activation depth $F_{n,j} = F_n$. They are thus all active within the total imaging window $z \in [F_n, F_f]$ and are equally focused. The size of the EA group is typically limited by a minimum element width criterion.

(ii) When the EA region is filled, elements are added outside. They have a multi-focus design with element j being active on receive within the region $z \in [F_{n,j}, F_f]$, where $F_{n,j+1} > F_{n,j}$, and F_f is the same as in (i). Elements are added as long as both the total number of elements and the total aperture size constraints are obeyed, and as long as $F_{n,j} < F_f$. The element radius and focusing for element $j+1$ are decided following either of the three below described focusing rules, selected depending on which rule that suits best given the values of $a_{o,j}$ and $F_{n,j+1}$.

A.2.2 Geometric pre-focusing rules

Constant-frequency (CF) pre-focusing

When considering a single element, the CF element pre-focusing rule is the same as given in [1]. CF pre-focusing is utilized when the receive frequency utilized is

constant within the whole imaging region $z \in [F_n, F_f]$. This is opposed to when attenuation decreases the penetration of high frequencies, which therefore are not utilized for transmissions intended to cover great depths.

If element j is designed for imaging within $z \in [F_{n,j}, F_f]$, its geometric pre-focus should be balanced so that the magnitude of the phase-shift is maximum at $z = F_{n,j}$ and $z = F_f$. Then $\Delta\varphi_j(F_{n,j}) = -\Delta\varphi_j(F_f)$ must be valid. Combining this with the phase-shift given by (A.1) yields the CF pre-focus rule:

$$F_j^{\mathrm{CF}} = \frac{2F_{n,j}F_f}{F_{n,j}+F_f} = F_{n,j}\frac{2\kappa_j}{1+\kappa_j}, \quad \text{for } \kappa_j \equiv F_f/F_{n,j}, \tag{A.5}$$

which is a scaling-factor introduced for further analysis of the pre-focusing rules presented.

Depth-dependent frequency (DDF) pre-focusing

The attenuation induced decrease of penetration depth with increasing frequency makes it inappropriate to use high frequencies at large depths in tissue. The DDF pre-focusing rule takes this into account. Following (A.4), one assumes that no shorter wavelength than $\lambda(z) = z/\chi$ is utilized beyond the depth z. This enables focusing closer to $F_{n,j}$. Hence the elements may be larger while still maintaining a maximum phase-shift equal to that of CF focusing.

Inserting (A.4) into (A.1), the phase-shift over element j at the depth z is then modified into its DDF version, for the remainder of the paper denoted $\Delta\varphi_j^{\chi}(z)$, with the wavelength $\lambda(z)$ increasing with z:

$$\Delta\varphi_j^{\chi}(z) = A_j\frac{\chi}{z}\left(\frac{1}{z}-\frac{1}{F_j}\right). \tag{A.6}$$

Similarly as for CF focusing, the phase-shifts are balanced: $\Delta\varphi_j^{\chi}(F_{n,j}) = -\Delta\varphi_j^{\chi}(F_f)$. Combining this with (A.6) and κ_j from (A.5), yields the DDF geometric pre-focus as shown in (A.17) of Tab. A.1.

Modified depth-dependent frequency (MDDF) pre-focusing

An analysis of $\Delta\varphi^{\chi}(z)$ as given in (A.6) shows that the phase-shift maximum magnitude for DDF pre-focusing occurs at the depth z_m:

$$z_m = 2F_j. \tag{A.7}$$

The depth z_m is inside the interval $z \in [F_{n,j}, F_f]$ only for $F_f > 2F_j$. If the inequality holds, even though $\Delta\varphi_j^{\chi}(z)$ is equal in magnitude at $F_{n,j}$ and F_f, there

exists a region within the imaging interval where its magnitude is larger. So when

$$\kappa_j F_{n,j} > 2F_{n,j}\kappa_j \frac{1+\kappa_j}{1+\kappa_j^2} \;\Leftrightarrow\; \kappa_j > 1+\sqrt{2}, \tag{A.8}$$

a modified approach is needed to make sure that $\Delta\varphi_j^{\chi}(z) \leq \theta$ within the whole interval $z \in [F_{n,j}, F_f]$.

A natural step is then to balance the geometric pre-focus so that

$$\Delta\varphi_j^{\chi}(F_n) = -\Delta\varphi_j^{\chi}(z_m). \tag{A.9}$$

Combining this with (A.6) and (A.7) then generates an equation which is solved to give the MDDF pre-focus, as shown in (A.18) of Tab. A.1.

Following (A.8), MDDF focusing is chosen instead of DDF when $\kappa_j > 1+\sqrt{2}$. Fig. A.2 shows a comparison between the CF, DDF, and MDDF focusing rules.

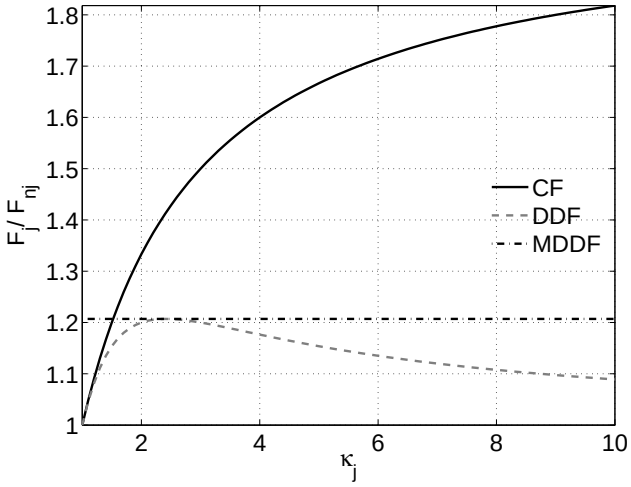

Figure A.2: Pre-focusing rules. Solid: F_j^{CF}, dashed: F_j^{DDF}, dashed-dotted: F_j^{MDDF}.

A.3.3 Element activation depth rules

The beamwidth $d(F_{n,j})$ at the element j activation depths $F_{n,j}$ is either regulated to be constant, or to in some way wary with increasing j. The following two beamwidth development variants are used to get rules for $F_{n,j+1}$ selection:

Constant CF beamwidth

If the receive frequency used is equal for all z, the beamwidth (A.3) at $z = F_{n,j+1}$, and constant beamwidth $d(F_{n,j+1}) = \hat{d}$ at the activation depth yields

$$F_{n,j+1} = \hat{d}a_{o,j}/\lambda. \tag{A.10}$$

Using the scaling relation $\kappa_j \equiv F_f/F_{n,j}$ then gives

$$\kappa_{j+1} = F_f\lambda/(\hat{d}a_{o,j}). \tag{A.11}$$

Linearly increasing DDF beamwidth

Here the maximum beamwidth within the depth-dependent frequency framework at the activation depth $F_{n,j+1}$ is set to grow linearly with z. A reason for this choice is that the beamwidth is inversely proportional to the frequency, while the frequency used for the DDF rule is inversely proportional to z. This is hence equal to a constant $F_\#$ at the element activation depths.

For a wavelength linearly increasing with the imaging depth, as in (A.4), the beamwidth estimate equation (A.3) changes to its DDF variant:

$$d^\chi(z) = \lambda(z)z/a_o(z) = z^2/\left(\chi a_o(z)\right). \tag{A.12}$$

If the maximum beamwidth at the activation depth where element j is inserted into the aperture is allowed to grow linearly, it has to fulfill

$$d^\chi(F_{n,j}) = B{\cdot}F_{n,j}, \tag{A.13}$$

where B is a dimensionless constant chosen depending on the desired $F_\#$ at $F_{n,j}$. The depth $F_{n,j+1}$ where element $j+1$ is inserted into the active receive aperture is thus the depth where the beamwidth estimate exceeds $d^\chi(z) = B \cdot z$ when elements $1 \ldots j$ are active and therefore the radius of the active receive aperture is $a_o(z) = a_{o,j}$. Combination of (A.12) for $z = F_{n,j+1}$ with (A.13) then yields

$$F_{n,j+1} = B\chi a_{o,j}, \tag{A.14}$$

which together with the definition of κ_j (A.5) leads to:

$$\kappa_{j+1} = F_f/\left(B\chi a_{o,j}\right), \tag{A.15}$$

This is thus equal to (A.11) if $\hat{d} = \lambda B\chi$.

Table A.1: Summary of the derived rules for geometric pre-focusing, and size of an added element $\#(j+1)$.

$$F_j^{\mathrm{CF}} = F_{n,j}\frac{2\kappa_j}{1+\kappa_j},\ a_{o,j+1}^{\mathrm{CF}} = \sqrt{\frac{2\lambda F_f\theta}{\pi}\frac{1}{\frac{F_f\lambda}{da_{o,j}}-1}+(a_{o,j}+w_k)^2} \tag{A.16}$$

$$F_j^{\mathrm{DDF}} = F_{n,j}\frac{\kappa_j(1+\kappa_j)}{1+\kappa_j^2},$$
$$a_{o,j+1}^{\mathrm{DDF}} = \sqrt{\frac{\theta F_f B a_{o,j}\left(\frac{F_f}{B\chi a_{o,j}}+1\right)}{\pi\left(\frac{F_f}{B\chi a_{o,j}}-1\right)}+(a_{o,j}+w_k)^2} \tag{A.17}$$

$$F_j^{\mathrm{MDDF}} = \frac{F_f}{\kappa_j}\frac{1+\sqrt{2}}{2},\ a_{o,j+1}^{\mathrm{MDDF}} = \sqrt{\frac{\theta F_f^2}{\pi\chi}\frac{1+\sqrt{2}}{1+\sqrt{2}-\frac{2F_f}{\chi a_{o,j}B}}+(a_{o,j}+w_k)^2} \tag{A.18}$$

$$F_j^{\text{BL-DDF}} = \frac{F_f F_{n,j}(F_f+\chi\lambda_{\mathrm{sh}})}{F_f^2+\chi\lambda_{\mathrm{sh}}F_{n,j}},\ a_{o,j+1}^{\text{BL-DDF}} = \sqrt{\tfrac{1}{\pi}\Big[(a_{o,j}+w_k)^2+\theta\lambda_{\mathrm{sh}}X\Big]}, \tag{A.19}$$

$$X \triangleq B\chi a_{o,j}\left[1-\frac{F_f^2+\chi^2\lambda_{\mathrm{sh}}Ba_{o,j}}{F_f(F_f+\chi\lambda_{\mathrm{sh}})}\right]^{-1}$$

$$F_j^{\text{BL-MDDF}} = \tfrac{1}{2}\left[F_{n,j}+\sqrt{F_{n,j}^2+\chi\lambda_{\mathrm{sh}}F_{n,j}}\right],$$
$$a_{o,j+1}^{\text{BL-MDDF}} = \sqrt{\tfrac{1}{\pi}\Big[(a_{o,j}+w_k)^2+\theta\lambda_{\mathrm{sh}}Y\Big]}, \tag{A.20}$$

$$Y \triangleq \left[\frac{1}{\iota a_{o,j}}-\frac{2}{\iota a_{o,j}+\sqrt{\left[\iota a_{o,j}\right]^2+\chi\lambda_{\mathrm{sh}}\iota a_{o,j}}}\right]^{-1}$$

A.4.4 Element size rules

CF element size

To formulate a rule for the outer aperture radius of element $j+1$ to be added to the aperture assuming the same frequency for all depths, CF focusing is combined with the element activation depth (A.15). Combination of (A.1) with (A.16) gives the phase-shift over the element to insert, evaluated at the outermost point F_f of the imaging window:

$$\Delta\varphi_{j+1}(F_f) = \frac{\pi A_{j+1}}{2\lambda F_f}\left(\kappa_{j+1} - 1\right). \tag{A.21}$$

Inserting (A.11) into (A.21) and writing the element area as

$$A_{j+1} = \pi\left[a_{o,j+1}^2 - (a_{o,j} + w_k)^2\right], \tag{A.22}$$

where w_k is the kerf between the elements, and setting the phase-shift over annulus $j+1$ to the given constraint $\Delta\varphi_{j+1}(F_f) = \theta$ generates the equation

$$\theta = \frac{\pi\left[a_{o,j+1}^2 - (a_{o,j} + w_k)^2\right]}{2\lambda F_f}\left(\frac{F_f\lambda}{\hat{d}a_{o,j}} - 1\right). \tag{A.23}$$

Solving this yields the outer aperture radius $a_{o,j+1}$ as given in (A.16) of Tab. A.1.

DDF element size

Using DDF focusing (A.17) and evaluating the phase-shift at $z = F_f$ from (A.6) leads to

$$\Delta\varphi_j^{\chi}(F_f) = \frac{A_j\chi}{F_f^2}\frac{\kappa_j(\kappa_j - 1)}{1 + \kappa_j}. \tag{A.24}$$

Inserting the element area (A.22), into (A.24) and setting $\Delta\varphi_{j+1}^{\chi}(F_f) = \theta$ generates

$$a_{o,j+1}^{\mathrm{DDF}} = \sqrt{\frac{\theta F_f^2}{\pi\chi\kappa_{j+1}}\frac{\kappa_{j+1} + 1}{\kappa_{j+1} - 1} + (a_{o,j} + w_k)^2}. \tag{A.25}$$

Insertion of κ_{j+1} for constant $F_\#$ from (A.15) into (A.25) yields the final DDF element size rule as shown in (A.17) of Tab. A.1.

MDDF element size

Using MDDF focusing (A.18) and evaluating the phase-shift at $z = F_f$ from (A.6) yields

$$\Delta\varphi_j^{\chi}(F_f) = A_j \frac{\chi}{F_f^2} \frac{1+\sqrt{2}-2\kappa_j}{1+\sqrt{2}}. \tag{A.26}$$

Setting the phase-shift at F_f to θ and inserting the expression for the element area A_{j+1} from (A.22), yields the outer radius of element $j+1$:

$$a_{o,j+1}^{\mathrm{MDDF}} = \sqrt{\frac{\theta F_f^2}{\pi\chi} \frac{1+\sqrt{2}}{1+\sqrt{2}-2\kappa_{j+1}} + (a_{o,j}+w_k)^2}. \tag{A.27}$$

Using κ_{j+1} for constant $F_\#$ (A.15), leads to the final MDDF element size rule as shown in (A.18) of Tab. A.1.

A.5.5 Frequency band limited multi-focus array

Physical transducers may only transmit and receive ultrasound pulses efficiently within some frequency band $f \in [f_{\mathrm{lo}}, f_{\mathrm{hi}}]$, corresponding to the wavelength band $\lambda \in [\lambda_{\mathrm{sh}}, \lambda_{\mathrm{lon}}]$. Taking this limited frequency band into account, the pre-focusing and element width rules may be adjusted so that the phase-shift over an element within $z \in [F_{n,j}, F_f]$ for the highest frequency that is ever used there $f \in [f_{\mathrm{lo}} = \chi c/F_f, f_{\mathrm{hi}} = \chi c/F_{n,j}]$ still does not exceed the limit θ. Therefore the total imaging region is divided into two zones:

1) Shallow depths $z \in [F_n, \chi\lambda_{\mathrm{sh}}]$ where the highest frequency used on receive is f_{hi}.

2) Great depths $z \in (\chi\lambda_{\mathrm{sh}}, \chi\lambda_{\mathrm{lon}}]$ where the highest frequency used on receive is a function of z: $f(z) = c\chi/z$.

For elements active both within Zone 1) and Zone 2), new geometric pre-focusing and element size rules may be formulated in order to take into consideration that the frequency in Zone 1) may never exceed f_{hi} due to the limited bandwidth. These adjusted focusing rules are here denoted band limited (BL) rules. Fig. A.3 displays the two depth zone extents.

Band limited DDF pre-focusing

For element j in the DDF case, the phase-shift $\Delta\varphi_j(F_{n,j})$ at the element activation depth has to be balanced to match the depth-dependent frequency phase-shift

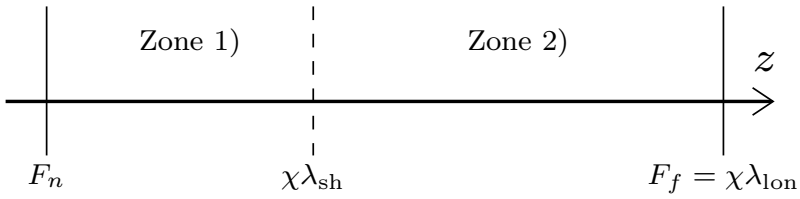

Figure A.3: Extents of Zone 1) and Zone 2) for the BL transducer case.

$\Delta\varphi_j^{\chi}(F_f)$ using (A.1) and (A.6):

$$\Delta\varphi_j(F_{n,j}) = -\Delta\varphi_j^{\chi}(F_f = \chi\lambda_{\mathrm{lon}}), \tag{A.28}$$

which yields the BL-DDF pre-focusing (A.19) shown of Tab. A.1.

Band limited MDDF pre-focusing

In the BL-MDDF case, the phase-shift $\Delta\varphi_j(F_{n,j})$ is balanced to match the depth-dependent frequency phase-shift $\Delta\varphi_j^{\chi}(z_m)$, where $z_m = 2F_j$ as in (A.7) is the depth where $\Delta\varphi_j^{\chi}(z \in [F_{n,j}, F_f])$ has its maximum. Then the phase-shift balancing equation is

$$\Delta\varphi_j(F_{n,j}) = -\Delta\varphi_j^{\chi}(2F_j). \tag{A.29}$$

Solving this for positive F_j yields the BL-MDDF focusing as given in (A.20) of Tab. A.1.

The MDDF version is used instead of the DDF version if $2F_j^{\text{BL-DDF}} > F_f$:

$$2F_f F_{n,j} \frac{F_f + \chi\lambda_{\mathrm{sh}}}{F_f^2 + \chi\lambda_{\mathrm{sh}} F_{n,j}} > F_f, \tag{A.30}$$

while BL-DDF pre-focusing is used elsewhere. Simplifying (A.30) shows that BL-MDDF focusing should be used if

$$F_{n,j} < \frac{F_f^2}{\chi\lambda_{\mathrm{sh}} + 2F_f}. \tag{A.31}$$

For elements that are active only within Zone 2), the previously described DDF or MDDF focusing rules (A.17) and (A.18) may be applied without modification.

Band limited element activation depth

Keeping $F_\#$ constant corresponds to having the beamwidth $d(F_{n,j})$ constant at the element activation depths within Zone 1), and to having the depth-dependent beamwidth $d^\chi(F_{n,j+1})$ linearly growing within Zone 2). This yields

$$\begin{array}{rll} d(F_{n,j+1}) & = \hat{d}, & z < \chi\lambda_{\text{sh}} \\ d^\chi(F_{n,j+1}) & = BF_{n,j+1}, & z \geq \chi\lambda_{\text{sh}} \end{array} \tag{A.32}$$

The beamwidth estimates when using elements $1...j$ for the wavelengths corresponding to Zone 1) and Zone 2) are

$$\begin{array}{rll} d(z) & = \frac{\lambda_{\text{sh}} z}{a_{o,j}(z)}, & z < \chi\lambda_{\text{sh}} \\ d^\chi(z) & = \frac{z^2}{\chi a_{o,j}(z)}, & z \geq \chi\lambda_{\text{sh}} \end{array} \tag{A.33}$$

Combining (A.32) with (A.33) and evaluating the expressions at the element activation depths $z = F_{n,j}$ both in Zone 1) and Zone 2) leads to

$$F_{n,j+1} = B\chi a_{o,j}, \tag{A.34}$$

which is similar to, For the remainder of this article this depth is called the BL element activation depth.

Band limited DDF element size

For elements which are active both within Zone 1) and Zone 2), combination of BL-DDF focusing (A.19), the BL element activation depth (A.34) and setting $\Delta\varphi(F_{n,j+1}) = \theta$ leads to

$$\theta = \frac{A_{j+1}}{\lambda_{\text{sh}}} \left(\frac{1}{B\chi a_{o,j}} - \frac{F_f^2 + \chi\lambda_{\text{sh}} B\chi a_{o,j}}{F_f B\chi a_{o,j}(F_f + \chi\lambda_{\text{sh}})} \right). \tag{A.35}$$

Combining the element area (A.22) with (A.35) yields a solution for $a_{o,j+1}$ as given in (A.20) of Tab. A.1.

Band limited MDDF element size

A similar calculation in case of BL-MDDF focusing (A.20), using the BL element activation depth (A.34) and setting $\Delta\varphi(F_{n,j+1}) = \theta$ yields

$$\theta = \frac{A_{j+1}}{\lambda_{\text{sh}}} \left(\frac{1}{\iota a_{o,j}} - \frac{2}{\iota a_{o,j} + \sqrt{(\iota a_{o,j})^2 + \chi\lambda_{\text{sh}} a_{o,j}}} \right),$$

where $\iota \equiv B\chi$. The outer radius of element $j+1$ then becomes as given in (A.20) of Tab. A.1.

A.4 Receive beam calculation method

Dynamically focused receive beams are simulated by use of an in-house implemented MATLAB code that solves the linear wave equation for a rotational symmetric geometry by forward propagation through the angular spectrum method with the Hankel Transform [17]. Because of the reciprocity of the wave equation, the receive beams are similar to the simulated transmit beams using the same aperture and focusing. The response is calculated for Continuous Waves (CW) at every frequency $1, 2, \ldots, 25\,\mathrm{MHz}$. Then RMS fields from pulses with Gaussian frequency distributions whose variance is half the center frequency are computed using Parseval's Theorem. Attenuation is taken into account by reduction of the response from each frequency by $0.5\,\mathrm{dB\,cm^{-1}MHz^{-1}}$.

To quantify the phase error effect on the beam sidelobes, each simulated beam is compared with the beam from an ideal dynamically focused aperture with no phase difference over it, and with the same active aperture radius at each depth as the multi-focus array. The ideal case beam profile is [16]

$$H(z,r) = K\frac{2J_1(ka_o(z)r/z)}{ka_o(z)r/z}, \tag{A.36}$$

where z is the depth, r the distance from the beam axis, K a depth-dependent amplitude constant, a_o the outer aperture radius, J_1 the Bessel function of the first kind and $k = 2\pi f/c$ the wave number. Attenuation inclusion and RMS total receive fields from pulses are generated similarly from calculated CW responses as for the simulated fields from an array. To simplify visual comparison, all beams are normalized before display to have the same amplitude at each depth. This ideal reference beam is below referred to as the ideal beam.

The sidelobe to mainlobe energy ratio is calculated as

$$E_r(z) = \frac{E_s(z)}{E_m(z)} = \frac{\int_r^\infty I(r',z)\,r'\mathrm{d}r'}{\int_0^r I(r',z)\,r'\mathrm{d}r'}, \tag{A.37}$$

where r' is the distance from the beam axis, r the mainlobe -15 dB outer limit, I the intensity, $E_s(z)$ the sidelobe energy, and $E_m(z)$ the mainlobe energy.

A.5 Results

A multi-focus array is designed using the BL method. The input parameters used are shown in Tab. A.2 while the resulting array is described graphically in Fig. A.4 and numerically in Tab. A.3. Estimated receive beamwidth and phase-shift over each element for the designed array are displayed in Fig. A.5. The resulting $F_\#$

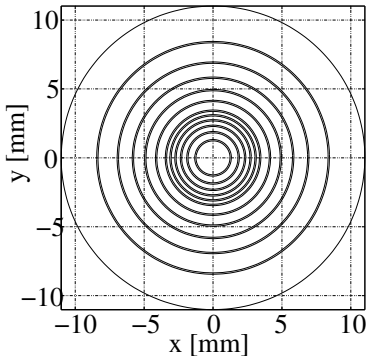

(a) Element sizes, with the thick lines placed in the middle of the kerf.

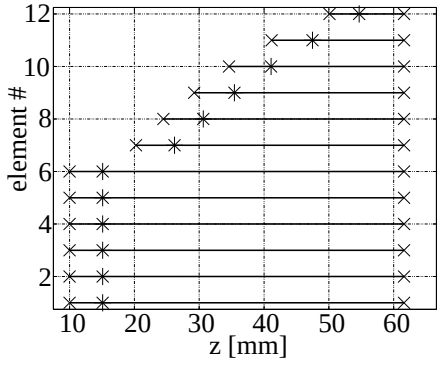

(b) Element active depths and foci. Left ×: $z = F_{n,j}$, right ×: $z = F_f$. Star: $z = F_j$.

Figure A.4: Resulting geometry using the BL method. Also shown in Tab. A.3.

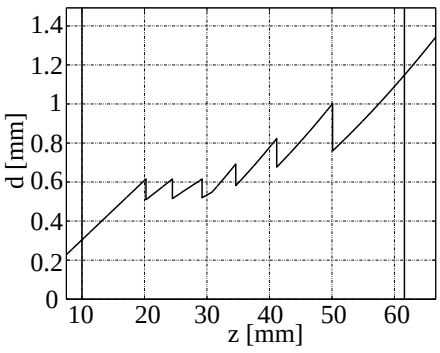

(a) Beamwidth as a function of depth using (A.3) and (A.12).

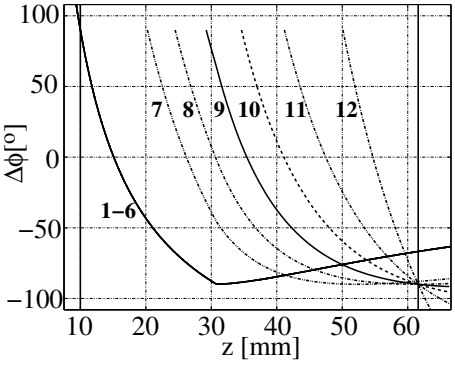

(b) Phase-shift over each element using (A.1) and (A.6). The bold numbers indicate element #.

Figure A.5: Beamwidth and phase-shift estimates. For both plots, the frequency is $f = f_{\text{hi}}$ where $z < 30.8\,\text{mm}$ (Zone 1), and depth-dependent like $f(z) = \chi c/z$ where $z > 30.8\,\text{mm}$ (Zone 2).

Table A.2: BL multi-focus design, input parameters. w_m is the min. allowed element width. F_f is given by $\chi c/f_{\mathrm{lo}}$.

c [m/s]	θ [°]	$\hat{d}$ [mm]	B	w_k [mm]	F_n [mm]	w_m [mm]	$f_{\mathrm{lo}}, f_{\mathrm{hi}}$ [MHz]	χ	F_f [mm]
1540	90	0.62	1/50	0.1	10	0.21	7.5, 15	300	61.6

Table A.3: Resulting multi-focus BL array. Lengths in mm, element area in mm^2. $a_{i,j}$ is the inner radius, and w_j is the element width.

j	$a_{i,j}$	$a_{o,j}$	w_j	A_j	$F_{n,j}$	F_j
1	0	1.23	1.23	4.8	10	15.1
2	1.33	1.82	0.49	4.8	10	15.1
3	1.92	2.28	0.36	4.8	10	15.1
4	2.38	2.68	0.30	4.8	10	15.1
5	2.78	3.04	0.26	4.8	10	15.1
6	3.14	3.37	0.23	4.7	10	15.1
7	3.47	4.08	0.61	14.5	20.2	26.2
8	4.18	4.87	0.69	19.6	24.5	30.6
9	4.97	5.77	0.80	27.0	29.2	35.4
10	5.87	6.86	0.99	39.6	34.6	41.1
11	6.96	8.35	1.4	66.9	41.2	47.5
12	8.45	11	2.6	155.8	50.1	54.7

is $\sim$3 at all points $F_{n,j}$. Simulated receive beams from the multi-focus array as well as corresponding ideal beams are displayed in Fig. A.6. Sidelobe to mainlobe energy ratios of these beams are presented in Fig. A.7.

As a reference an EA array is designed with the same number of elements, total aperture size, frequency, F_n and $F_f = \chi\lambda_{\mathrm{lon}}$ as for the multi-focus array of Tab. A.3. The outermost and thinnest element gets 0.41 mm wide in the resulting geometry. The phase-shift estimate (A.1) over the elements gives $\Delta\varphi_j(F_n) = -\Delta\varphi(F_f) = 322°$ for all j. Simulated receive beams for this EA array and from its corresponding ideal beams are shown in Fig. A.8. The corresponding sidelobe to mainlobe energy ratios are presented in Fig. A.9.

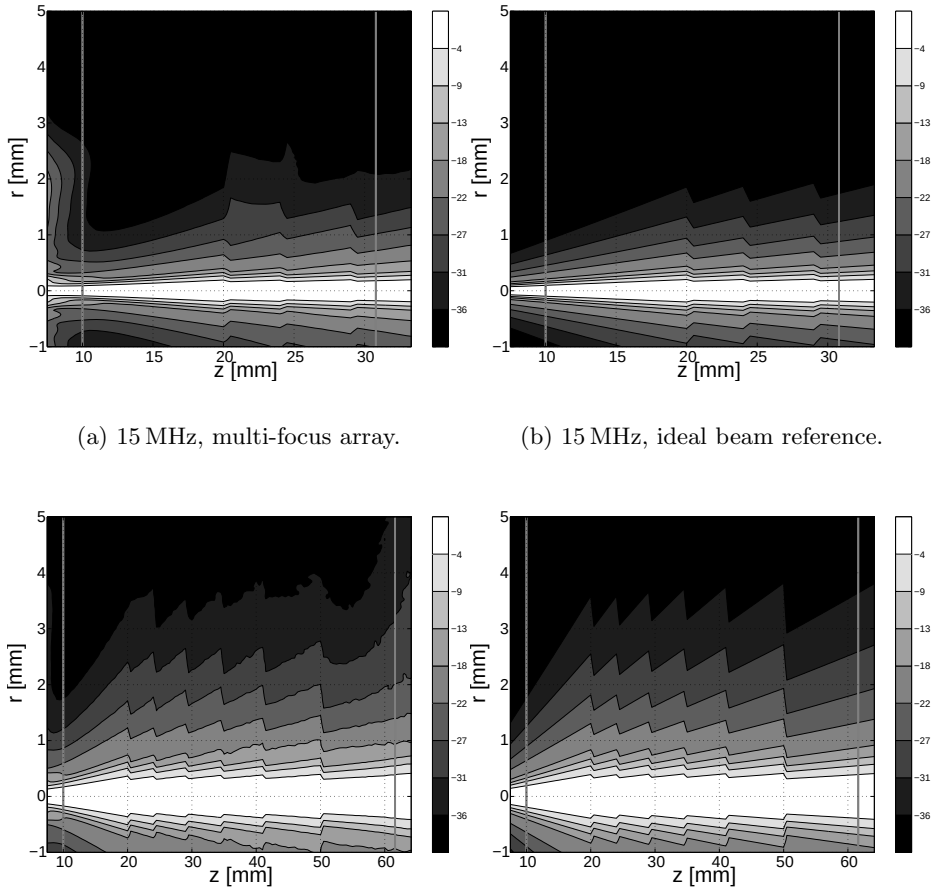

(a) 15 MHz, multi-focus array.

(b) 15 MHz, ideal beam reference.

(c) 7.5 MHz, multi-focus array.

(d) 7.5 MHz, ideal beam reference.

Figure A.6: Resulting beams using the array presented in Tab. A.3, and the corresponding ideal beams. Pressure in dB, normalized at each depth. Note that the z scale differs between the 7.5 and 15 MHz cases.

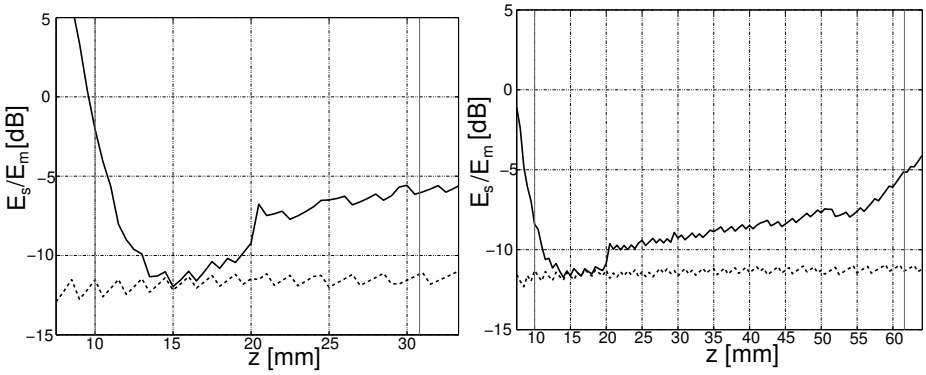

(a) 15 MHz.

(b) 7.5 MHz.

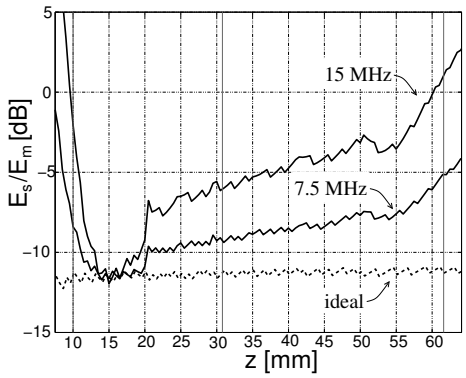

(c) Sum up: 7.5 and 15 MHz in the same plot.

Figure A.7: Sidelobe to mainlobe energy ratio in the receive beams. Solid lines: beams from designed multi-focus array. Dashed lines: reference ideal beams. Vertical lines: imaging region limits $F_n = 10\,\text{mm}$, $F_f = \chi\lambda_{\text{lon}}$.

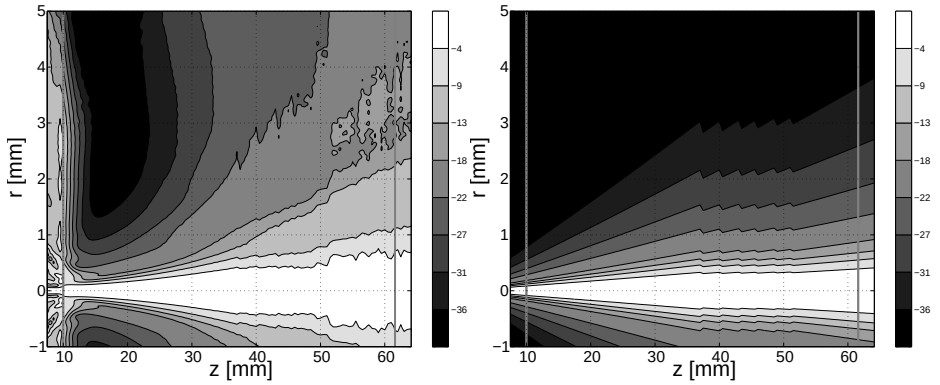

(a) Equal area array.

(b) Ideal beam reference.

Figure A.8: Resulting receive beams, 12 elements EA array, and corresponding ideal beams at $f = 7.5\,\text{MHz}$. Pressure normalized at each depth.

A.6 Discussion

The depth-dependent frequency framework presented in this paper is introduced in order to take into account that the highest frequency suitable for imaging decreases with increasing imaging depth. It should not be confused with the less pronounced center frequency decrease of a propagating pulse caused by greater attenuation of high than of low frequencies. Multi-focus arrays may also be designed without the depth-dependent frequency rules, utilizing the constant-frequency focusing and element sizes. For a given aperture and imaging window, this results in a larger number of and thinner elements. But the elements are still wider and fewer than for EA design.

The presented multi-focus array is for $[7.5, 15]\,\text{MHz}$, but the presented design rules may be adapted to arrays using other frequency intervals.

The receive beam simulations for Gaussian pulses with center frequencies at 7.5 and 15 MHz give beamwidths that are kept below a wavelength-dependent limit within the depths $z \in [F_n, \chi\lambda]$. The estimated sidelobe to mainlobe energy ratios are below $\sim -7\,\text{dB}$ within the imaging window of each frequency. For the ideal reference beam, the sidelobe to mainlobe energy ratio is $\sim -12\,\text{dB}$.

The beams from a comparison 12 element EA array focused at 17.2 mm, displayed in Fig. A.8, indicate an imaging window being much shorter than for the

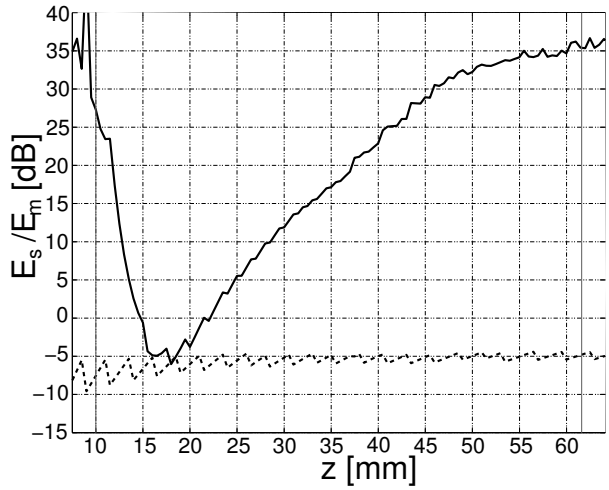

Figure A.9: Sidelobe to mainlobe energy ratio in the beams of Fig. A.8. Solid line: EA array beam. Dashed line: ideal beam. Vertical lines: imaging region limits $F_n = 10\,\text{mm}$, $F_f = \chi\lambda_{\text{lon}}$.

multi-focus array due to high sidelobe to mainlobe energy ratio caused by large phase-shifts, as displayed in Fig. A.9. If instead an EA array is designed to get similar efficiency as for the presented multi-focus design having $\theta = 90°$, the same kerf, pre-focus, frequency and aperture, it needs 42 elements with the narrowest element being only 0.07 mm wide. The two comparison EA designs thus suffer from either a short imaging window or a large number of thin elements.

The sudden $\sim$3 dB increase in sidelobe to mainlobe energy ratio at $z = 20.2\,\text{mm}$ for beams from the designed multi-focus array is due to insertion of the first non-central group element into the active aperture. The element has its $\Delta\varphi_j(F_{n,j}) = \theta$ at this depth. All annuli active at depths inferior of 20.2 mm are pre-focused to 15.1 mm thus contributing with a small phase-shift around this depth.

The axial resolution for a 15 MHz pulse is approx. [4]

$$d_z \sim \frac{cT_p}{2} \approx \frac{c}{2\beta} \approx 0.2\,\text{mm}, \tag{A.38}$$

where T_p is the pulse length and $\beta = 33\%$ the frequency bandwidth. Thus the lateral and axial resolutions for the designed multi-focus array are of the same order, therefore facilitating reconstruction of any-plane cuts from a three-dimensional data volume.

A.7 Concluding remarks

The article presents a geometric pre-focusing method which allows annular arrays to combine a large imaging window and a high frequency with a large aperture.

Array design rules presented in case of limited transducer frequency bandwidth are used to design an array which operates at $f \in [7.5, 15]$ MHz. The receive imaging windows for the two frequencies cover $z \in [10, 61]$ respectively $z \in [10, 31]$ mm for the lowest and highest frequencies. The outcome is an array of 12 elements with a central always-active zone of 6 elements. The total aperture diameter is 22 mm, corresponding to $\sim 100\lambda$ at 7.5 MHz. The active aperture at 31 mm depth, the deepest point from where 15 MHz is received, also corresponds to $\sim 100\lambda$ at the given frequency.

The flexibility and capabilities of an annular array probe may be improved using arrays defined using the presented multi-focus design method. This design principle may be advantageous for high resolution applications needing simultaneous high frequency, large aperture, and large imaging window.

Multi-focus array manufacturing is more complex than single pre-focus manufacturing. For example the array has to be precisely centered to make the elements fit onto the appropriate pre-focus region. An equal-area design generally results in equal element impedances thus requiring the same circuit and power consumption for each element, while the multi-focus array may demand more intricate electronic circuits. A way to reduce the number of pre-foci needed and the electronic circuit complexity is to group the elements *e.g.* pairwise or in triplets with equal pre-focus and equal area.

To ultimately test the design method, future work within the field should include experimental validation and development of manufacturing methods, as well as investigation of clinical benefits.

References

[1] M. Arditi, F. S. Foster, and J. W. Hunt, "Transient fields of concave annular arrays," *Ultrason. Imag.*, vol. 3, pp. 37–61, 1981.

[2] D. H. Turnbull, B. G. Starkoski, K. A. Harasiewicz, G. R. Lockwood, and F. S. Foster, "Ultrasound backscatter microscope for skin imaging," in *Proc. IEEE Ultrason. Symp.*, Baltimore, MD, Oct./Nov. 1993, pp. 985–988.

[3] F. S. Foster, G. R. Lockwood, L. K. Ryan, K. A. Harasiewicz, L. Berube, and A. M. Rauth, "Principles and applications of ultrasound backscatter microscopy," *IEEE Trans. Ultrason., Ferroelect., Freq. Contr.*, vol. 40, no. 5, pp. 608–617, Sept. 1993.

[4] M. Arditi, W. B. Taylor, F. S. Foster, and J. W. Hunt, "An annular array system for high resolution breast echography," *Ultrasonic Imaging*, vol. 4, pp. 1–31, 1982.

[5] J. F. Lynch, "Some simple expressions for the beamforming properties of focused high-resolution circular arrays, with applications to refocusing systems," *J. Acoust. Soc. Am.*, vol. 74, no. 3, pp. 847–850, 1983.

[6] H. E. Melton and F. L. Thurstone, "Annular array design and logarithmic processing for ultrasonic imaging," *Ultrasound Med. Biol.*, vol. 4, pp. 1–12, 1978.

[7] R. B. Bernardi, P. J. Peluso, R. J. O'Connell, S. Kellog, and C. Shih, "A dynamically focused annular array," in *Proc. IEEE Ultrason. Symp.*, ser. 76, 1976, pp. 157–159.

[8] H. Mhanna, B. Trummer, C. M. Kargel, and M. F. Insana, "Ultrasonic annular array system for detecting tissue motion," in *Medical Imaging 2002: Ultrasonic Imaging and Signal Processing*, vol. 4687. SPIE, 2002, pp. 171–181.

[9] J. A. Brown, C. E. M. Demore, and G. R. Lockwood, "Design and fabrication of annular arrays for high-frequency ultrasound," *IEEE Trans. Ultrason., Ferroelect., Freq. Contr.*, vol. 51, no. 8, pp. 1010–1017, Aug. 2004.

[10] J. A. Ketterling, O. Aristizabal, D. H. Turnbull, and F. L. Lizzi, "Design and fabrication of a 40-MHz annular array transducer," *IEEE Trans. Ultrason., Ferroelect., Freq. Contr.*, vol. 52, no. 4, pp. 672–681, Apr. 2005.

[11] O. Aristizabal, J. A. Ketterling, and D. H. Turnbull, "40-mhz annular array imaging of mouse embryos," *Ultrasound Med. Biol.*, vol. 32, no. 11, pp. 1631–1637, 2006.

[12] K. A. Snook, C.-H. Hu, T. R. Shrout, and K. K. Shung, "High-frequency ultrasound annular-array imaging. Part I: array design and fabrication," *IEEE Trans. Ultrason., Ferroelect., Freq. Contr.*, vol. 53, no. 2, pp. 300–308, Feb. 2006.

[13] C.-H. Hu, K. A. Snook, P.-J. Cao, and K. K. Shung, "High-frequency ultrasound annular array imaging. Part II: digital beamformer design and imaging," *IEEE Trans. Ultrason., Ferroelect., Freq. Contr.*, vol. 53, no. 2, pp. 309–316, Feb. 2006.

[14] E. J. Gottlieb, J. M. Cannata, C.-H. Hu, and K. K. Shung, "Development of a high-frequency (> 50 MHz) copolymer annular-array, ultrasound transducer," *IEEE Trans. Ultrason., Ferroelect., Freq. Contr.*, vol. 53, no. 5, pp. 1037–1045, May 2006.

[15] W. Yuan, S. A. Johnson, M. J. Berggren, and R. S. Eidens, "A concave annular array design, based on phasor summation – Part I: design methodology," *Ultrasonic Imaging*, vol. 10, pp. 275–286, 1988.

[16] B. A. J. Angelsen, *Ultrasound imaging. Waves, Signals and Signal Processing.* Trondheim, Norway: Emantec, 2000, vol. 1, ch. 5.6B, http://www.ultrasoundbook.com.

[17] P. T. Christopher and K. J. Parker, "New approaches to the linear propagation of acoustic fields," *J. Acoust. Soc. Amer.*, vol. 90, pp. 507–521, 1991.

Paper B,C and D
are not included due to copyright

Bibliography

B. Angelsen. *Ultrasound imaging. Waves, signals and signal processing*, volume I. Emantec, Trondheim, 2000. http://www.ultrasoundbook.com.

B. Angelsen. *Ultrasound imaging. Waves, signals and signal processing*, volume II. Emantec, Trondheim, 2000. http://www.ultrasoundbook.com.

B. A. J. Angelsen and R. Hansen. SURF imaging – a new method for ultrasound contrast agent imaging. In *Proc. IEEE Ultrason. Symp.*, pages 531–541, New York, NY, USA, Oct. 2007.

B. A. J. Angelsen, T. F. Johansen, and L. Hoff. Simulation of gas bubble scattering for large mach-numbers. In *Proc. IEEE Ultrason. Symp.*, volume 1, pages 505–508, Caesars Tahoe, NV, USA, 1999.

M. Arditi, F. S. Foster, and J. W. Hunt. Transient fields of concave annular arrays. *Ultrason. Imag.*, 3:37–61, 1981.

M. Arditi, W. B. Taylor, F. S. Foster, and J. W. Hunt. An annular array system for high resolution breast echography. *Ultrasonic Imaging*, 4:1–31, 1982.

O. Aristizabal, J. A. Ketterling, and D. H. Turnbull. 40-mhz annular array imaging of mouse embryos. *Ultrasound Med. Biol.*, 32(11):1631–1637, 2006.

M. A. Averkiou. Tissue harmonic imaging. In *Proc. IEEE Ultrason. Symp.*, pages 1553–1572, 2000.

M. A. Averkiou, D. N. Roundhill, and J. E. Powers. A new imaging technique based on the nonlinear properties of tissue. In *Proc. IEEE Ultrason. Symp.*, pages 1561–1566, 1997.

R. B. Bernardi, P. J. Peluso, R. J. O'Connell, S. Kellog, and C. Shih. A dynamically focused annular array. In *Proc. IEEE Ultrason. Symp.*, 76, pages 157–159, 1976.

R. T. Beyer. Parameter of nonlinearity in fluids. *J. Acoust. Soc. Am.*, 32 (6):719–721, 1960.

S. Bloch, P. Dayton, and K. Ferrara. Targeted imaging using ultrasound contrast agents. *IEEE Eng. Med. Biol.*, 23(5):18–29, Sep.–Oct. 2004.

A. Bouakaz and N. de Jong. New contrast imaging method using double frequency exposure. In *2004 IEEE Ultrason. Symp.*, volume 1, pages 339–342, Aug. 23–27, 2004.

A. Bouakaz, M. Versluis, J. Borsboom, and N. de Jong. Radial modulation of microbubbles for ultrasound contrast imaging. *IEEE Trans. Ultrason. Ferroelectr., Freq. Contr.*, 54(11):2283–2290, Nov. 2007.

J. A. Brown, C. E. M. Demore, and G. R. Lockwood. Design and fabrication of annular arrays for high-frequency ultrasound. *IEEE Trans. Ultrason., Ferroelect., Freq. Contr.*, 51(8):1010–1017, Aug. 2004.

K. Caidahl, E. Kazzam, J. Lidberg, G. Neumann-Andersen, J. Nordanstig, S. R. Dahlqvist, A. Waldenstrom, and R. Wikh. New concept in echocardiography: harmonic imaging of tissue without use of contrast agent. *The Lancet*, 352:1264–1270, 1998.

W.-S. Chen, T. J. Matula, A. A. Brayman, and L. A. Crum. A comparison of the fragmentation thresholds and inertial cavitation doses of different ultrasound contrast agents. *J. Acoust. Soc. Am.*, 113(1):643–651, Jan. 2003.

J. Chomas, P. Dayton, J. Allen, K. Morgan, and K. Ferrara. Mechanisms of contrast agent destruction. *IEEE Trans. Ultrason. Ferroelectr. Freq. Control*, 48(1):232–248, Jan. 2001.

S. Choudhry, B. Gorman, J. Charboneau, D. Tradup, R. Beck, J. Kofler, and D. Groth. Comparison of tissue harmonic imaging with conventional us in abdominal disease. *Radiographics*, 20(4):1127–1135, 2000.

P. T. Christopher and K. J. Parker. New approaches to the linear propagation of acoustic fields. *J. Acoust. Soc. Amer.*, 90:507–521, 1991.

T. Christopher. Finite amplitude distortion-based inhomogeneous pulse echo ultrasonic imaging. *IEEE Trans. Ultrason., Ferroelectr., Freq. Contr.*, 44(1):125–139, Jan. 1997.

T. Christopher. Experimental investigation of finite amplitude distortion-based, second harmonic pulse echo ultrasonic imaging. *IEEE Trans. Ultrason., Ferroelectr., Freq. Contr.*, 45(1):158–162, Jan. 1998.

D. Cosgrove. Ultrasound contrast agents: An overview. *Eur. J. Radiol.*, 60:324–330, Dec. 2006.

N. de Jong, R. Cornet, and C. T. Lancée. Higher harmonics of vibrating gas-filled microspheres. Part one: Simulations. *Ultrasonics*, 32(6):447–453, 1994.

N. de Jong, R. Cornet, and C. T. Lancée. Higher harmonics of vibrating gas-filled microspheres. Part two: Measurements. *Ultrasonics*, 32(6):455–459, 1994.

C. X. Deng, F. L. Lizzi, A. Kalisz, A. Rosado, R. H. Silverman, and D. J. Coleman. Study of ultrasonic contrast agents using a dual-frequency band technique. *Ultrasound Med. Biol.*, 26:819–831, 2000.

C. H. Desch, D. O. Sproule, and W. J. Dawson. The detection of cracks in steel by means of supersonic waves. *J. Iron Steel Inst.*, 153:319–327, 1946.

T. S. Desser, R. B. J. Jeffrey, M. J. Lane, and P. W. Ralls. Tissue harmonic imaging: Utility in abdominal and pelvic sonography. *J. Clin. Ultrasound*, 27(3):135–142, 1999.

T. S. Desser, T. Jesrzejewicz, and C. Bradley. Native tissue harmonic imaging: Basic principles and clinical applications. *Ultrasound Quart*, 16 (40):40–48, 2002.

T. J. Dubinsky, C. Cuevas, M. K. Dighe, O. Kolokythas, and J. H. Hwang. High-intensity focused ultrasound: Current potential and oncologic applications. *Am. J. Roentgenol.*, 190(1):191–199, Jan. 2008.

F. A. Duck. *Physical properties of tissue.* Academic Press, 1990.

F. A. Duck. Nonlinear acoustics in diagnostic ultrasound. *Ultrasound Med. Biol.*, 28(1):1–18, 2002.

K. D. Evans, B. Weiss, and M. Knopp. High-intensity focused ultrasound (HIFU) for specific therapeutic treatments: A literature review. *J. Diagn. Med. Sonog.*, 23(6):319–327, 2007.

R. J. Fedewa, K. D. Wallace, M. R. Holland, J. R. Jago, G. C. Ng, M. R. Rielly, B. S. Robinson, and J. G. Miller. Spatial coherence of the nonlinearly generated second harmonic portion of backscatter for a clinical imaging system. *IEEE Trans. Ultrason., Ferroelectr., Freq. Contr.*, 50(8): 1010–1022, Aug. 2003.

R. J. Fedewa, K. D. Wallace, M. R. Holland, J. R. Jago, G. C. Ng, M. R. Rielly, B. S. Robinson, and J. G. Miller. Spatial coherence of backscatter for the nonlinearly produced second harmonic for specific transmit apodizations. *IEEE Trans. Ultrason., Ferroelectr., Freq. Contr.*, 51(5):576–588, May 2004.

F. A. Firestone. The supersonic reflectoscope, an instrument for inspecting the interior of solid parts by means of sound waves. *J. Acoust. Soc. Am.*, 17(3):287–299, Jan. 1946.

F. S. Foster, G. R. Lockwood, L. K. Ryan, K. A. Harasiewicz, L. Berube, and A. M. Rauth. Principles and applications of ultrasound backscatter microscopy. *IEEE Trans. Ultrason., Ferroelect., Freq. Contr.*, 40(5):608–617, Sept. 1993.

P. J. A. Frinking and N. de Jong. Acoustic modeling of shell-encapsulated gas bubbles. *Ultrasound Med. Biol.*, 24:523–533, May 1998.

D. E. Goertz, M. E. Frijlink, N. de Jong, and A. F. W. van der Steen. Dual frequency microbubble imaging for high frequency ultrasound systems. In *Proc. IEEE Ultrason. Symp.*, Vancouver, BC, Canada, Oct. 2006.

E. J. Gottlieb, J. M. Cannata, C.-H. Hu, and K. K. Shung. Development of a high-frequency ($>$ 50 MHz) copolymer annular-array, ultrasound transducer. *IEEE Trans. Ultrason., Ferroelect., Freq. Contr.*, 53(5):1037–1045, May 2006.

R. Hansen. *New techniques for Detection of Ultrasound Contrast Agents*. PhD thesis, Norwegian University of Science and Technology, 2004.

G. R. Harris. Transient field of a baffled planar piston having an arbitrary vibration amplitude distribution . *J. Acoust. Soc. Am.*, 70:186–204, July 1981.

W. R. Hedrick and L. Metzger. Tissue harmonic imaging: A review. *J. Diagn. Med. Sonog.*, 21(3):183–189, 2005.

W. R. Hedrick and C. L. Peterson. Image artifacts in real-time ultrasound. *J. Diagn. Med. Sonog.*, 11(6):300–308, 1995.

L. M. Hinkelman, D.-L. Liu, L. A. Metlay, and R. C. Waag. Measurements of ultrasonic pulse arrival time and energy level variations produced by propagation through abdominal wall. *J. Acoust. Soc. Am.*, 95(1):530–541, 1994.

L. M. Hinkelman, T. D. Mast, L. A. Metlay, and R. C. Waag. The

effect of abdominal wall morphology on ultrasonic pulse distortion. Part I: Measurements. *J. Acoust. Soc. Am.*, 104(6):3635–3649, 1998.

L. Hoff. Nonlinear response of sonazoid. Numerical simulations of pulse-inversion and subharmonics. *2000 IEEE Ultrason. Symp.*, 2:1885–1888, Oct. 2000.

L. Hoff, P. C. Sontum, and J. M. Hovem. Oscillations of polymeric microbubbles: Effect of the encapsulating shell. *J. Acoust. Soc. Am.*, 107(4):2272–2280, 2000.

C.-H. Hu, K. A. Snook, P.-J. Cao, and K. K. Shung. High-frequency ultrasound annular array imaging. Part II: digital beamformer design and imaging. *IEEE Trans. Ultrason., Ferroelect., Freq. Contr.*, 53(2):309–316, Feb. 2006.

P. Jiang, Z. Mao, and J. Lazenby. A new tissue harmonic imaging scheme with better fundamental frequency cancellation and higher signal-to-noise ratio. In *Proc. IEEE Ultrason. Symp.*, volume 2, pages 1589–1594, 1998.

Y. Jing and R. O. Cleveland. Modeling the propagation of nonlinear three-dimensional acoustic beams in inhomogeneous media. *J. Acoust. Soc. Am.*, 122(3):1352–1364, 2007.

G. Jones. Echolocation. *Curr. Biol.*, 15:R484–R488, July 2005.

C. F. Keogh and P. L. Cooperberg. Is it real or is it an artifact. *Ultrasound Q.*, 17(4):201–210, Dec. 2001.

J. A. Ketterling, O. Aristizabal, D. H. Turnbull, and F. L. Lizzi. Design and fabrication of a 40-MHz annular array transducer. *IEEE Trans. Ultrason., Ferroelect., Freq. Contr.*, 52(4):672–681, Apr. 2005.

D. B. Khismatullin. Resonance frequency of microbubbles: Effect of viscosity. *J. Acoust. Soc. Am.*, 116(3):1463–1473, 2004.

E. Klaseboer and B. C. Khoo. A modified rayleigh-plesset model for a non-spherically symmetric oscillating bubble with applications to boundary integral methods. *Eng. Anal. Bound. Elem.*, 30:59–71, 2006.

T. Kling, K. K. Shung, and G. A. Thieme. Reverberation reduction in ultrasonic b-mode images via dual frequency image subtraction. *IEEE Transactions on Medical Imaging*, 12(4):792–802, 1993.

D. Kourtiche, L. A. Ali, A. Chitnalah, and M. Nadi. Theoretical study of harmonic generation sound beams in case of uniform, exponential and cosinusoidal apertures. *Proc. 23rd Annual EMBS Int. Conf., Istanbul, Turkey*, 3:2395–2398, 2001.

F. W. Kremkau and K. J. Taylor. Artifacts in ultrasound imaging. *J. Ultrasound. Med.*, 5(4):227–237, 1986.

T. G. Leighton. What is ultrasound? *Prog. Biophys. Mol. Biol.*, 93:3–83, 2007.

Lord Rayleigh. On the pressure developed in a liquid during the collapse of a spherical cavity. *Philos. Mag.*, 34:94–98, 1917.

J. F. Lynch. Some simple expressions for the beamforming properties of focused high-resolution circular arrays, with applications to refocusing systems. *J. Acoust. Soc. Am.*, 74(3):847–850, 1983.

K. Mahmutyazicioglu, H. A. Tanriverdi, H. Ozdemir, A. Barut, H. Davsanci, and S. Gundogdu. Transabdominal pulse inversion harmonic imaging improves assesment of ovarian morphology in virgin patients with pcos: comparison with conventional b-mode sonography. *Eur. J. Radiol.*, 53(2): 208–286, Feb. 2005.

T. D. Mast, A. I. Nachman, and R. C. Waag. Focusing and imaging using eigenfunctions of the scattering operator. *J. Acoust. Soc. Am.*, 102(2): 715–725, Aug. 1997.

H. Mhanna, B. Trummer, C. M. Kargel, and M. F. Insana. Ultrasonic annular array system for detecting tissue motion. In *Medical Imaging 2002: Ultrasonic Imaging and Signal Processing*, volume 4687, pages 171–181. SPIE, 2002.

H. E. Melton and F. L. Thurstone. Annular array design and logarithmic processing for ultrasonic imaging. *Ultrasound Med. Biol.*, 4:1–12, 1978.

K. Morgan, M. Averkiou, and K. Ferrara. The effect of the phase of transmission on contrast agent echoes. *IEEE Trans. Ultrason. Ferroelectr. Freq. Control*, 45(4):872–875, July 1998.

S.-E. Måsøy, T. F. Johansen, and B. Angelsen. Correction of ultrasonic wave aberration with a time delay and amplitude filter. *J. Acoust. Soc. Am.*, 113(4):2009–2020, Apr. 2003.

S.-E. Måsøy, Ø. Standal, P. Näsholm, T. F. Johansen, R. Hansen, and B. Angelsen. SURF imaging: In vivo demonstration of an ultrasound contrast agent detection technique. *IEEE Trans. Ultrason. Ferroelectr., Freq. Contr.*, 2008. Accepted for publishing.

S.-E. Måsøy, T. Varslot, and B. Angelsen. Iteration of transmit-beam aberration correction in medical ultrasound imaging. *J. Acoust. Soc. Am.*, 117(1):450–461, 2005.

G. C. Ng, S. S. Worrell, P. D. Freiburger, and G. E. Trahey. A comparative evaluation of several algorithms for phase aberration correction. *IEEE Trans. Ultrason. Ferroelectr. Freq. Control*, 41(5):631–643, Sept. 1994.

L. F. Nock, G. E. Trahey, and S. W. Smith. Phase aberration correction in medical ultrasound using speckle brightness as an image quality factor. *J. Acoust. Soc. Am.*, 85(5):1819–1833, May 1989.

M. O'Donnell. Coded excitation system for improving the penetration of real-time phased-array imaging systems. *IEEE Trans. Ultrason., Ferroelectr., Freq. Contr.*, 39(3):341–351, May 1992.

M. Plesset. The dynamics of cavitation bubbles. *J. Appl. Mech.*, 16: 277–282, 1949.

E. Quaia. Microbubble ultrasound contrast agents: an update. *Eur. Radiol.*, 17:1995–2008, 2007.

K. A. Scanlan. Sonographic artifacts and their origins. *Am. J. Roentgenol.*, 156(6):1267–1272, June 1991.

H. H. Shariff, P. D. Bevan, R. Karshafian, R. Williams, and P. N. Burns. Radial modulation imaging: Raising the frequency for contrast imaging. In *Proc. IEEE Ultrason. Symp.*, pages 104–107, Vancouver, BC, Canada, Oct. 2006.

C.-C. Shen and P.-C. Li. Harmonic leakage and image quality degradation in tissue harmonic imaging. *IEEE Trans. Ultrason., Ferroelectr., Freq. Contr.*, 48(3):728–736, May 2001.

C.-C. Shen and P.-C. Li. Motion artifacts of pulse inversion-based tissue harmonic imaging. *IEEE Trans. Ultrason., Ferroelectr., Freq. Contr.*, 49 (9):1203–1211, Sept. 2002.

A. Shmulewitz, S. A. Teefey, and B. S. Robinson. Factors affecting image quality and diagnostic efficacy in abdominal sonography: A prospective study of 140 patients. *J. Clin. Ultrasound*, 21(9):623–630, 1993.

D. Simpson and P. Burns. Pulse inversion doppler: a new method for detecting nonlinear echoes from microbubble contrast agents. *1997 IEEE Ultrason. Symp.*, 2:1597–1600, Oct. 1997.

K. A. Snook, C.-H. Hu, T. R. Shrout, and K. K. Shung. High-frequency ultrasound annular-array imaging. Part I: array design and fabrication. *IEEE Trans. Ultrason., Ferroelect., Freq. Contr.*, 53(2):300–308, Feb. 2006.

M. Tabei, T. D. Mast, and R. C. Waag. Simulation of ultrasonic focus

aberration and correction through human tissue. *J. Acoust. Soc. Am.*, 113 (2):1166–1176, 2003.

J. D. Thomas and D. N. Rubin. Tissue harmonic imaging: why does it work? *J. Am. Soc. Echocardiogr.*, 11(8):803–808, 1998.

D. H. Turnbull, B. G. Starkoski, K. A. Harasiewicz, G. R. Lockwood, and F. S. Foster. Ultrasound backscatter microscope for skin imaging. In *Proc. IEEE Ultrason. Symp.*, pages 985–988, Baltimore, MD, Oct./Nov. 1993.

T. Varslot, H. Krogstad, E. Mo, and B. Angelsen. Eigenfunction analysis of stochastic backscatter for characterization of acoustic aberration in medical ultrasound imaging. *J. Acoust. Soc. Am.*, 115(6):3068–3076, June 2004.

T. Varslot, S.-E. Måsøy, and B. A. Angelsen. Aberration and second harmonic imaging. In *Proc. IEEE Ultrason. Symp.*, volume 2, pages 1327–1330, Sept. 18–21, 2005.

T. Varslot, S.-E. Måsøy, T. F. Johansen, and B. Angelsen. Aberration in nonlinear acoustic wave propagation. *IEEE Trans. Ultrason., Ferroelectr., Freq. Contr.*, 54(3):470–479, Mar. 2007.

T. Varslot and G. Taraldsen. Computer simulation of forward wave propagation in soft tissue. *IEEE Trans. Ultrason. Ferroelectr. Freq. Control*, 52(9):1473–1482, 2005.

K. D. Wallace, M. R. Holland, B. S. Robinson, R. J. Fedewa, C. W. Lloyd, and J. G. Miller. Impact of propagation through an aberrating medium on the linear effective apodization of a nonlinearly generated second harmonic field. *IEEE Trans. Ultrason., Ferroelectr., Freq. Contr.*, 53(7):1260–1268, July 2006.

B. Ward, A. C. Baker, and V. F. Humphrey. Nonlinear propagation applied to the improvement of resolution in diagnostic medical ultrasound. *J. Acoust. Soc. Am.*, 101(1):143–154, 1997.

K. Wei, A. R. Jayaweera, S. Firoozan, A. Linka, D. M. Skyba, and S. Kaul. Quantification of myocardial blood flow with ultrasound-induced destruction of microbubbles administered as a constant venous infusion. *Circulation*, 97:473–483, Feb. 1998.

P. N. T. Wells. Ultrasound imaging. *Phys. Med. Biol.*, 51:R83–R98, June 2006.

W. Yuan, S. A. Johnson, M. J. Berggren, and R. S. Eidens. A concave annular array design, based on phasor summation – Part I: design methodology. *Ultrasonic Imaging*, 10:275–286, 1988.